nature metabolism

ARTICLES

https://doi.org/10.1038/s42255-021-00457-w

Check for updates

# Mesenteric lymphatic dysfunction promotes insulin resistance and represents a potential treatment target in obesity

Enyuan Cao[1,2]✉, Matthew J. Watt[3], Cameron J. Nowell[4], Tim Quach[1,2], Jamie S. Simpson[2,5], Vilena De Melo Ferreira[1], Sonya Agarwal[1], Hannah Chu[1], Anubhav Srivastava[1], Dovile Anderson[1], Gracia Gracia[1,2], Alina Lam[1], Gabriela Segal[6,7], Jiwon Hong[8,9], Luojuan Hu[1,2], Kian Liun Phang[8,9], Alistair B. J. Escott[8,9], John A. Windsor[8,9,10], Anthony R. J. Phillips[8,9], Darren J. Creek[1], Natasha L. Harvey[11], Christopher J. H. Porter[1,2]✉ and Natalie L. Trevaskis[1]✉

**Visceral adipose tissue (VAT) encases mesenteric lymphatic vessels and lymph nodes through which lymph is transported from the intestine and mesentery. Whether mesenteric lymphatics contribute to adipose tissue inflammation and metabolism and insulin resistance is unclear. Here we show that obesity is associated with profound and progressive dysfunction of the mesenteric lymphatic system in mice and humans. We find that lymph from mice and humans consuming a high-fat diet (HFD) stimulates lymphatic vessel growth, leading to the formation of highly branched mesenteric lymphatic vessels that 'leak' HFD-lymph into VAT and, thereby, promote insulin resistance. Mesenteric lymphatic dysfunction is regulated by cyclooxygenase (COX)-2 and vascular endothelial growth factor (VEGF)-C–VEGF receptor (R)3 signalling. Lymph-targeted inhibition of COX-2 using a glyceride prodrug approach reverses mesenteric lymphatic dysfunction, visceral obesity and inflammation and restores glycaemic control in mice. Targeting obesity-associated mesenteric lymphatic dysfunction thus represents a potential therapeutic option to treat metabolic disease.**

Lymphatic vasculature is essential for dietary lipid absorption, fluid homoeostasis and immune surveillance[1–4] and contributes to the pathogenesis of cancers[5,6], inflammatory diseases[4,7,8] and neurodegenerative diseases[9–13]. Recently, Zhang et al. demonstrated that blocking dietary lipid transport via the initial lymphatics (lacteals) in intestinal villi protects against obesity[14]. Here we now show a major role for mesenteric lymphatics in the development of insulin resistance in obesity.

Obesity is associated with significant impairments in lymphatic function in peripheral tissues[15–21], and adipose tissue accumulates around the site of lymph leakage in humans with lymphedema[22,23] and in transgenic mice with malformed lymphatics[24–27]. Excessive accumulation of VAT, which wraps around internal organs and mesenteric lymphatics that drain the gut, leads to excess release of fatty acids and adipokines from VAT that promote insulin resistance in glucoregulatory tissues[28–30]. By contrast, accumulation of subcutaneous adipose tissue (SAT), which is associated with peripheral lymphatics beneath the skin, is not a risk factor for insulin resistance[28–30]. Importantly, the mesenteric lymph fluid that courses through VAT is enriched in gut-derived lipid metabolites and pro-inflammatory mediators when compared to the peripheral lymph in SAT[31]. Mesenteric lymphatic vessel permeability and contractility are also altered in genetically diabetic (*db*/*db*) mice[32] and rats fed a high-fructose diet[33]. Previously, Kuan et al. showed that the inherent permeability of collecting lymphatic vessels in the mesentery and periphery enables distribution of lymph components to surrounding adipose tissue[34]. We thus hypothesized that dysfunction of mesenteric lymphatics and, in particular, the leakage of HFD-modified mesenteric lymph into VAT promotes the accumulation of VAT and insulin resistance.

Herein, we demonstrate that mesenteric lymphatics become dysfunctional during the progression of HFD-induced obesity in mice and in humans with obesity. Notably, HFD-modified lymph fluid 'leaks' into VAT, promoting VAT accumulation and insulin resistance. We show that COX-2 and VEGF-C signalling via VEGFR3 regulate obesity-associated mesenteric lymphatic dysfunction and that lymph-targeted inhibition of COX-2 using a glyceride prodrug of celecoxib effectively reverses mesenteric lymphatic dysfunction and improves obesity and glycaemic control. Together, our findings lead us to propose that mesenteric lymphatic dysfunction contributes to visceral obesity and insulin resistance, thereby uncovering a potential treatment strategy for metabolic disease: targeted restoration of mesenteric lymphatic function.

[1]Drug Delivery, Disposition and Dynamics, Monash Institute of Pharmaceutical Sciences, Parkville, Victoria, Australia. [2]ARC Centre of Excellence in Convergent Bio-Nano Science and Technology, Monash Institute of Pharmaceutical Sciences, Parkville, Victoria, Australia. [3]Department of Physiology, University of Melbourne, Parkville, Victoria, Australia. [4]Drug Discovery Biology, Monash Institute of Pharmaceutical Sciences, Parkville, Victoria, Australia. [5]Puretech Health, Boston, MA, USA. [6]Department of Biochemistry and Molecular Biology, Bio21 Molecular Science and Biotechnology Institute, University of Melbourne, Parkville, Victoria, Australia. [7]Biological Optical Microscopy Platform, Bio21 Molecular Science and Biotechnology Institute, University of Melbourne, Parkville, Victoria, Australia. [8]Applied Surgery and Metabolism Laboratory, School of Biological Sciences, University of Auckland, Auckland, New Zealand. [9]Surgical and Translational Research Centre, University of Auckland, Auckland, New Zealand. [10]HBP/Upper GI Unit, Department of General Surgery, Auckland City Hospital, Auckland, New Zealand. [11]Centre for Cancer Biology, University of South Australia and SA Pathology, Adelaide, South Australia, Australia. ✉e-mail: enyuan.cao@monash.edu; chris.porter@monash.edu; natalie.trevaskis@monash.edu

## Results

**Mesenteric lymphatic remodelling in HFD-induced obesity.** First, we evaluated structural alterations in lymphatic vessels, villi and fat-associated lymphoid clusters (FALCs)[35,36] during the progression of obesity in mice fed an HFD versus those fed a control fat diet (CFD) for 6, 15, 23 or 32 weeks. We also examined lymphatic vessel structure in the VAT of human patients who were either lean or presented with obesity. In the duodenum, both villi and lacteals were significantly wider, and the villi, but not lacteals, were shorter in mice after 15 weeks of HFD feeding (Extended Data Fig. 1a–e). Mesenteric lymphatic vessels in VAT became progressively more branched with HFD feeding (Fig. 1a,b). The increase in vessel branching was not significant at week 6 of HFD feeding but became significant at week 15 and was most pronounced at week 32. In humans with obesity, increased lymphatic vessel branching was confirmed through measurement of vessel tortuosity, which showed a ~35% decrease in straighter vessels (tortuosity ratio, 0.93–1) and a ~50% increase in tortuous vessels (0.8–0.87) in VAT from humans with obesity compared to humans who were lean (Fig. 1c,d and Extended Data Fig. 1h (individual replicates)). In both mice fed the HFD and humans with obesity, lymphatic vessels appeared disorganized and tortuous rather than following the direction of lymph flow (Fig. 1a–d).

FALCs have not previously been evaluated in obesity. We found that the number of FALCs increased significantly after 15 and 32 weeks of HFD feeding (Fig. 1e,f). In obesity, FALCs mostly retained structural characteristics reported previously[35,36] including blood vessels, T cells, B cells and macrophages (Extended Data Fig. 1i–m). However, we found that some FALCs, particularly those in obese mice, contained tortuous lymphatic vessels (Fig. 1g, left) that have not been described previously and occasionally interconnected to an adjacent FALC and/or to branched lymphatic vessels in VAT to form a complex lymphatic network (Fig. 1g, right). Together, these data provide evidence of substantial lymphatic remodelling in VAT in HFD-induced obesity.

**Mesenteric lymph leaks to VAT in HFD-induced obesity.** To assess the drainage and transport function of mesenteric lymphatic vessels, we next conducted Evans blue dye lymphangiography experiments in mice fed a CFD or HFD for 6, 15 or 32 weeks. Evans blue dye was injected into the intestinal mucosa, and dye drainage from the injection site via the initial lymphatic vessels, transport through to collecting lymphatic vessels and leakage to surrounding VAT was visualized and quantified over time. After 6 weeks of HFD feeding, lymphatic drainage was efficient and there was no significant change in dye leakage from lymphatic vessels (Fig. 2a). However, lymph leakage increased significantly after 15 weeks of HFD feeding and became more substantial after 32 weeks of HFD feeding (Fig. 2b,c). Remarkably, in some cases of chronic HFD feeding, lymph leakage resulted in no transport of blue-dyed lymph via collecting lymphatics beyond the leaky point (Fig. 2c(i)), suggesting almost complete redirection into VAT. Notably, although lymph leakage to VAT occurred at various points along lymphatic vessels, it occurred most frequently around highly branched and disorganized regions (Fig. 2b(iv),c(iv)).

To further examine whether mesenteric lymphatic dysfunction results from HFD feeding or the development of obesity, we assessed mesenteric lymphatic structure and function in *db*/*db* mice that develop obesity and diabetes on a normal CFD. Despite developing significant obesity, *db*/*db* mice fed the CFD lacked both lymphatic vessel branching and lymph leakage and displayed similar lymph immune cell counts as those of lean C57BL/6 mice fed the CFD (Extended Data Fig. 2a–f). Further, *db*/*db* mice accumulated substantially more SAT (more than twofold), while mesenteric adipose tissue weight was comparable to that of mice fed the HFD, suggesting that *db*/*db* mice are more prone to peripheral fat deposition (Extended Data Fig. 2g). Importantly, this suggests that mesenteric lymphatic remodelling is dependent on HFD consumption and that data from *db*/*db* mice do not recapitulate lymphatic changes observed in humans in whom obesity is usually driven by diet.

**Lymph leakage promotes VAT accumulation and insulin resistance.** We hypothesized that leakage of HFD-modified mesenteric lymph (HFD-lymph) promotes VAT accumulation and insulin resistance. To mimic lymph leakage to VAT, lymph from rats fed the CFD and HFD was characterized for lipid metabolites, titrated and co-incubated with 3T3-L1 adipocytes (Extended Data Fig. 3a–e). Incubation of mature 3T3-L1 adipocytes in vitro with 2% (vol/vol) HFD-lymph significantly increased intracellular accumulation of lipid droplets and triglycerides (TGs) in adipocytes, relative to incubation with control medium and 2% (vol/vol) CFD-lymph (significant for lipid droplets only) (Fig. 3a–c). Expression of adipogenic genes including *Pparg*, *Lep* and *Gapdh*, but not that of *Cebpa*, was significantly increased in 3T3-L1 cells when exposed to HFD-lymph, but not CFD-lymph, relative to that from control medium during adipogenesis (Fig. 3d). mRNA expression of *Pnpla2* (gene encoding the lipolysis enzyme ATGL) was also higher following exposure of adipocytes to HFD-lymph but not CFD-lymph compared to that from control medium (Fig. 3d). Importantly, CFD-lymph does not leak into VAT in vivo; thus, there would be limited effect on adipogenesis as compared to that from HFD-lymph. This is supported by data showing that upregulation of adipogenesis genes was dependent on lymph concentration (Extended Data Fig. 3f). Consistent with the increase in lipolytic enzyme expression, HFD-lymph increased basal and forskolin (protein kinase A)-stimulated lipolysis relative to control medium and forskolin-stimulated lipolysis compared to CFD-lymph (Fig. 3e). In further experiments, we found that the main lymph components that stimulate lipolysis are in lipid-rich chylomicron and very low-density lipoprotein fractions (Extended Data Fig. 3g). This is consistent with data demonstrating that lipid and chylomicron fractions of lymph promote adipogenesis[25,37].

As disproportionate increases in adipose tissue lipolysis and the subsequent release of free fatty acids (FFAs) promote insulin resistance in vivo[38] and insulin action in peripheral tissues is an important determinant of glycaemic control[39], we next assessed whether lymph leakage into VAT impairs insulin sensitivity. We measured basal and insulin-stimulated $^{14}$C-2-deoxyglucose ($^{14}$C-2DG) uptake into 3T3-L1 adipocytes in vitro in the presence of CFD-lymph, HFD-lymph or control medium and in VAT explants isolated from around leaky or non-leaky lymphatics ex vivo. Remarkably, insulin-stimulated $^{14}$C-2DG uptake into 3T3-L1 adipocytes (Fig. 3f) and human adipocytes (Extended Data Fig. 3h) was significantly impaired after treatment with HFD-lymph compared to that from control medium and CFD-lymph (for 3T3-L1 adipocytes). Insulin-stimulated $^{14}$C-2DG uptake was also significantly impaired in VAT isolated from mice fed the HFD compared to that from mice fed the CFD and was most impaired in VAT isolated from around leaky versus non-leaky lymphatics in mice fed the HFD (Fig. 3g,h). HFD-lymph leakage to VAT thus promotes insulin resistance in local VAT, which may contribute to systemic insulin resistance.

**COX-2 and VEGF-C regulate lymphatic function and glucose tolerance.** HFD-lymph therefore contains factors that promote VAT accumulation and insulin resistance. Next, we assessed whether HFD-lymph also contains factors that promote mesenteric lymphatic vessel branching and leakiness. We first confirmed that HFD-lymph from mice and fed lymph from a human who was overweight are pro-lymphangiogenic, as shown by an increase in lymphatic endothelial cell (LEC) closure of a scratch wound in vitro upon incubation with 2% (vol/vol) lymph relative to that from control medium (Fig. 4a–d).

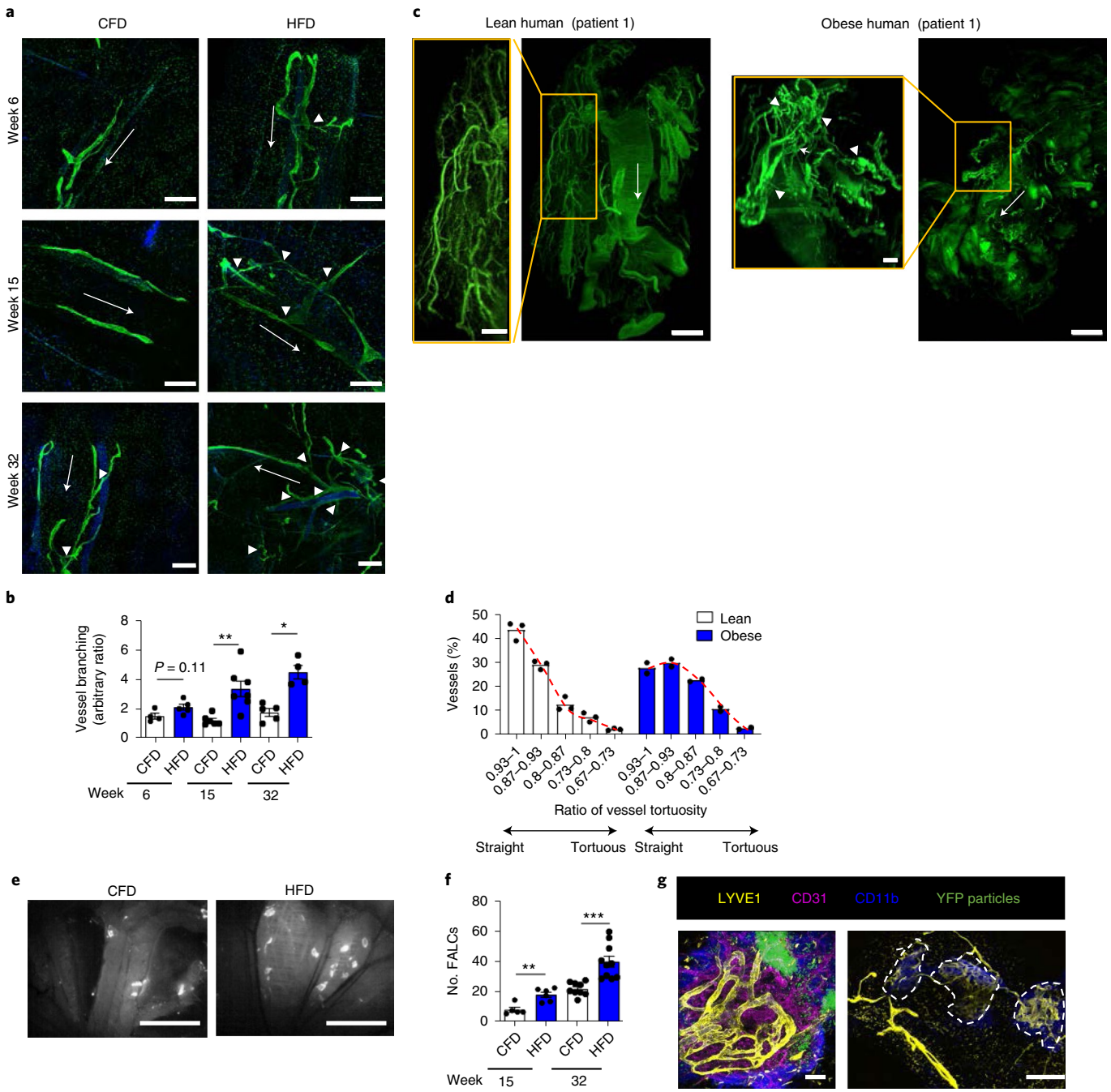


**Fig. 1 | HFD-induced obesity is associated with progressive mesenteric lymphatic remodelling. a**, Representative immunofluorescence images of mesenteric lymphatic vessels (lymphatic vessel endothelial hyaluronan receptor (LYVE)1 (green) and Hoechst (blue)) in VAT of mice fed the HFD or CFD for 6, 15 or 32 weeks. White arrows show vessel branches. Scale bars, 500 µm. Note that white arrows indicate the direction of lymph flow; arrowheads indicate points of vessel branching. **b**, Quantification of mesenteric lymphatic vessel branching in VAT of mice after 6, 15 or 32 weeks of CFD or HFD feeding. Mean ± s.e.m., $n = 4$ or 5 for week 6, $n = 6$ or 7 for week 15 and $n = 4$ or 5 for week 32. **c**, Representative images of podoplanin$^+$ lymphatic vessels (green) in mesenteric adipose tissue from humans who were lean or obese. Note that white arrows indicate the direction of lymph flow; arrowheads indicate points of increased vessel tortuosity. Scale bars, 500 µm (lean) and 1,000 µm (obese) and 200 µm in magnified images. Three-dimensional (3D) projections are available in Supplementary Fig. 2. **d**, Quantification of mesenteric lymphatic vessel tortuosity in mesenteric adipose tissue of humans who were lean or obese. The *x* axis shows the ratio of vessel tortuosity (1, straight; <1, tortuous; degree of tortuosity is divided into five categories; mean of $n = 3$ or 2). **e**, Representative fluorescent images showing FALCs in VAT of mice fed the CFD or HFD, identified by uptake of YFP fluorescent nanospheres administered intraperitoneally (seen as white dots). Scale bars, 500 µm. **f**, Total number of FALCs in VAT of mice fed the HFD or CFD for 15 or 32 weeks. Mean ± s.e.m. for $n = 5$ or 6 mice for week 15 and $n = 9$ or 10 mice for week 32. **g**, Representative immunofluorescence images of two to three FALCs from $n = 5$ mice showing LYVE1$^+$ lymphatic vessels (yellow), CD31$^+$ blood vessels (purple), CD11b$^+$ myeloid cells (blue) and YFP fluorescent nanospheres (green). **g**, Left, lymphatic vessels and blood vessels in a single FALC. **g**, Right, three separate FALCs (circled by white dashed lines) connected by an extensive lymphatic network. Scale bars, 100 µm (**g**, left) and 500 µm (**g**, right). Representative of images from two to three FALCs for $n = 5$ mice. Statistical differences, $^*P < 0.05$, $^{**}P < 0.01$ and $^{***}P < 0.005$ from two-tailed Student's *t*-tests except for data from **b** for weeks 6 and 32 (a two-tailed Mann–Whitney test was used). *P* values and details of statistical testing are provided as source data.

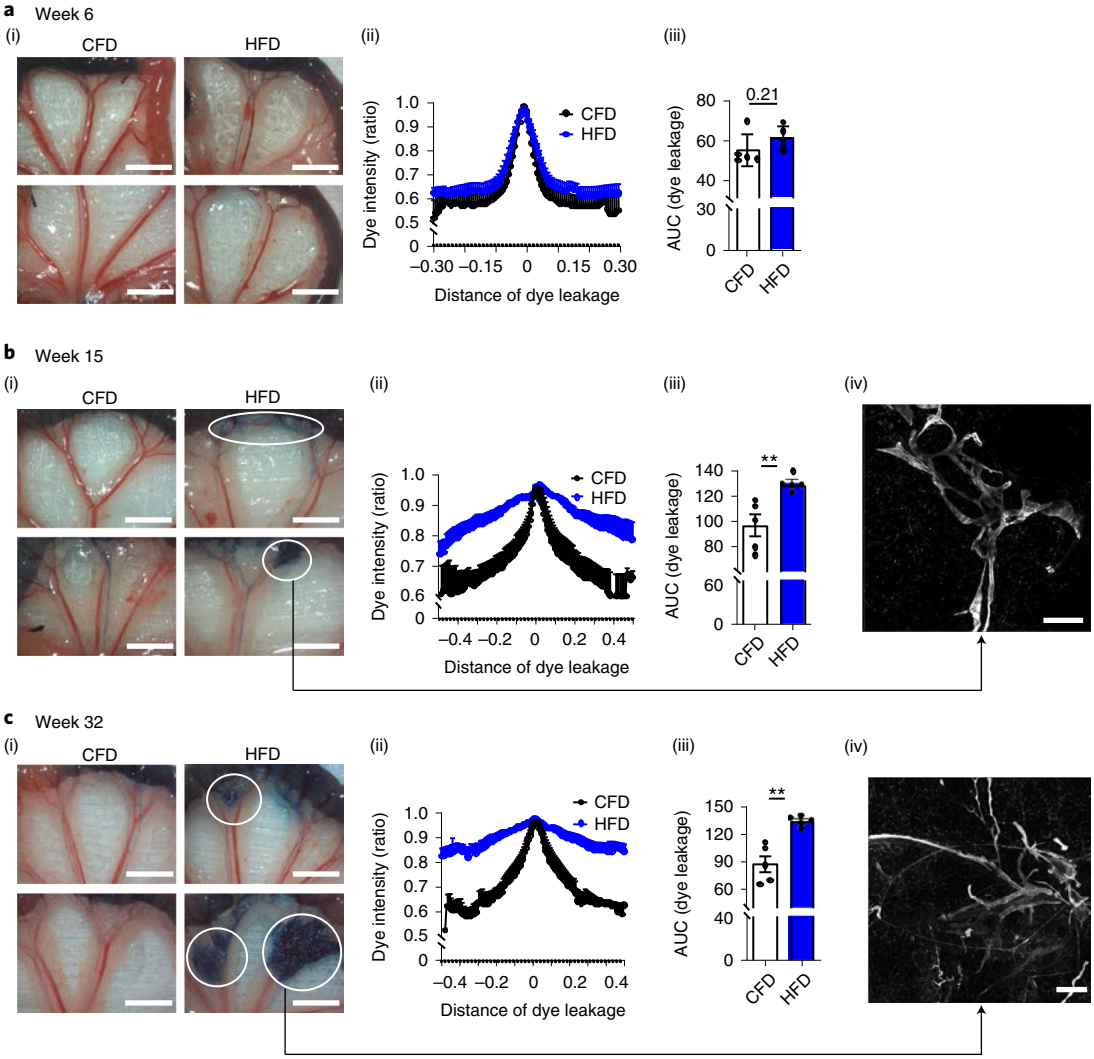


**Fig. 2 | Mesenteric lymphatic remodelling in HFD-induced obesity results in lymph 'leakage' to VAT. a–c**, Data for week 6, 15 or 32 of CFD or HFD feeding, respectively. **a**(i),**b**(i),**c**(i), Representative images of Evans blue dye passage through mesenteric lymphatic vessels and leakage to VAT 10 min after intramucosal dye injection. Scale bar, 5 mm. White circles show sites of extensive lymph leakage. **a**(ii),**b**(ii),**c**(ii), Quantification of lymph leakage to VAT. Graphs show Evans blue dye intensity at the centre of the vessel (peak) outward to VAT (lowest point of lines). Mean ± s.e.m. for $n = 5$ mice for weeks 6, 15 and 32. **a**(iii),**b**(iii),**c**(iii), Area under the curve (AUC) of Evans blue dye intensity plots. Mean ± s.e.m. for $n = 5$ mice for weeks 6, 15 and 32. **b**(iv),**c**(iv), Representative immunofluorescence images of lymphatic vessels in VAT (LYVE1 (grey)) showing that lymphatic vessels are highly branched at sites of lymph leakage (regions imaged in **b**(iv),**c**(iv) are areas circled in white in **b**(i),**c**(i), respectively, and are connected by black arrows). Scale bars in **b**(iv) and **c**(iv), 100 µm and 500 µm, respectively. Statistical differences, $^{*}P < 0.05$ or $^{**}P < 0.01$ from two-tailed Student's *t*-tests. *P* values and details of statistical testing are provided as source data.

The most important mediator of lymphangiogenesis in development and disease is VEGF-C signalling via VEGFR3. In the setting of cancer, prostaglandin E2 (PGE2) synthesized by the COX-2 enzyme also regulates lymphangiogenesis by recruiting or stimulating VEGF-C release from macrophages[40,41]. COX-2 inhibitors[42,43] and VEGF-C–VEGFR3 inhibitors[44,45] reduce obesity and insulin resistance; although these effects were previously assumed to result from anti-inflammatory actions. We hypothesized that COX-2–PGE2 and VEGF-C–VEGFR3 signalling regulates obesity-associated mesenteric lymphatic dysfunction and, as a result, insulin resistance. To first assess this in vitro, we confirmed that LEC migration induced by HFD-lymph was inhibited by the COX-2 inhibitor celecoxib, the VEGFR3 kinase inhibitor MAZ51 (Fig. 4b) and LY3127760, an antagonist of the prostaglandin EP4 receptor (Extended Data Fig. 4a).

To test our hypothesis in vivo, we administered the COX-2 inhibitor celecoxib (29 mg per kg per day, mixed with HFD, timeline in Fig. 4e; prevention study) to mice for 15 weeks. The concentration of VEGF-C in mesenteric lymph increased with 15 weeks of HFD feeding (Fig. 4f), and celecoxib treatment led to a significant reduction in PGE2 levels in lymph but not that of VEGF-C ($P = 0.15$) (Fig. 4f,g). Consistent with these results, celecoxib administration effectively prevented the increase in mesenteric lymphatic vessel branching and leakiness (Fig. 4h–k). In mice fed the HFD, we also observed increases in immune cell accumulation in mesenteric lymph and lymph nodes that were prevented in the mesenteric lymph fluid but not lymph nodes by celecoxib administration (Extended Data Fig. 5a–f). Importantly, these protective effects of celecoxib were associated with an improvement in oral glucose tolerance; although no significant differences in fasting blood glucose ($P = 0.06$) or body weight were observed for this celecoxib-dosing regime (Fig. 4l–n). These data support the hypothesis that inhibition of COX-2–PGE2 and VEGF-C–VEGFR3 signalling attenuates

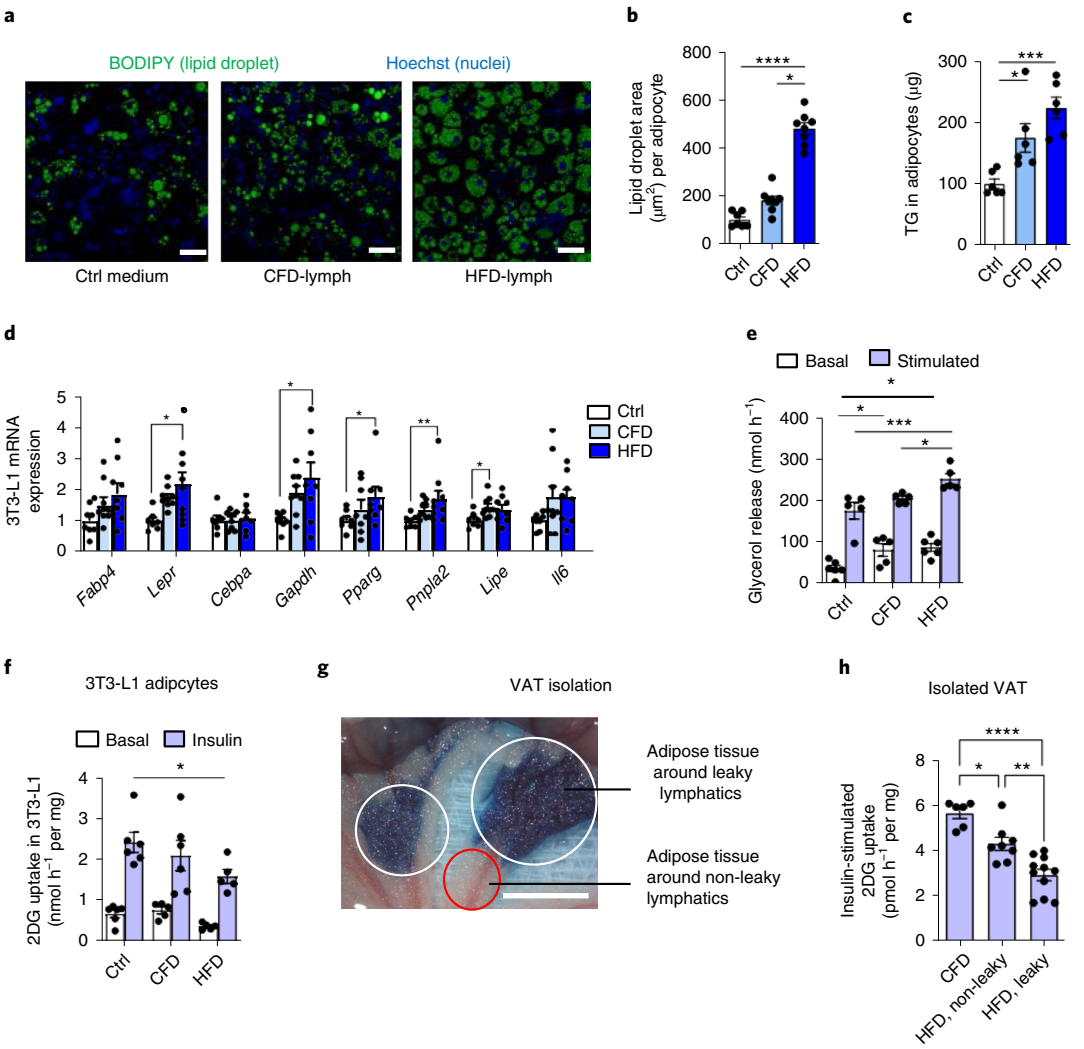


**Fig. 3 | Mesenteric lymph leakage into VAT promotes adipocyte differentiation, lipid accumulation and insulin resistance. a–f**, Data for 3T3-L1 adipocytes treated with control (ctrl) medium or 2% (vol/vol) CFD-lymph (CFD) or HFD-lymph (HFD) in medium. **a**, Lipid droplets (BODIPY, green) in mature adipocytes (nuclei, blue). Scale bar, 100 μm. **b**, Average adipocyte area occupied by lipid droplets. Mean ± s.e.m. for $n = 7$ (control), $n = 8$ (CFD) and $n = 8$ (HFD). **c**, Mass of intracellular TG in adipocytes. Mean ± s.e.m. for $n = 6$ (control), $n = 6$ (CFD) and $n = 6$ (HFD) from $N = 2$ experiments. **d**, Real-time PCR analysis of *Fabp4*, *Lepr*, *Cebpa*, *Gapdh*, *Pparg*, *Pnpla2*, *Lipe* and *Il6* mRNA expression in adipocytes. Mean ± s.e.m. for *Fabp4* ($n = 8, 9, 9$), *Lepr* ($n = 7, 9, 9$), *Cebpa* ($n = 7, 9, 8$), *Gapdh* ($n = 8, 9, 8$), *Pparg* ($n = 7, 8, 8$), *Pnpla2* ($n = 7, 9, 9$), *Lipe* ($n = 7, 8, 8$) and *Il6* ($n = 8, 9, 8$) from $N = 3$ experiments. **e**, Lipolysis in mature adipocytes (from glycerol release) in basal and forskolin-stimulated conditions. Mean ± s.e.m. for $n = 6$, 5 or 6 (basal) and $n = 5$, 5 or 5 (forskolin) replicates from $N = 2$ experiments. **f**, Uptake of $^{14}$C-2DG (2DG) into mature 3T3-L1 adipocytes in basal and insulin-stimulated conditions. Mean ± s.e.m. for $n = 6$, 5 or 5 (basal) and $n = 6$, 6 or 5 (insulin) replicates of $N = 2$ experiments. **g**, Microphotograph showing example sites where VAT was isolated adjacent to leaky (white circle) or non-leaky (red circle) lymphatics. Scale bar, 5 mm. **h**, Insulin-stimulated $^{14}$C-2DG uptake into VAT isolated from mice fed the CFD or HFD adjacent to leaky lymphatics or non-leaky lymphatics. Mean ± s.e.m. for $n = 6$, 7 or 9 mice. Statistical differences, $^{*}P < 0.05$, $^{**}P < 0.01$, $^{***}P < 0.005$ or $^{****}P < 0.001$ from two-way ANOVA (**e**,**f**) and one-way ANOVA (**b**–**d**,**h**). *P* values and details of statistical testing are provided as source data.

HFD-associated mesenteric lymphatic branching, lymph leakage and glucose intolerance.

**Lymph-targeted COX-2 inhibition reverses lymphatic dysfunction by reducing local VEGF-C release.** To further test the potential to reverse visceral obesity and insulin resistance through targeted restoration of mesenteric lymphatic function, we next conducted a treatment study. Mice were fed an HFD for 15 weeks to induce moderate lymphatic branching, lymph leakage, obesity and insulin resistance (as shown in Fig. 4h–n) and then treated with either celecoxib or, in an attempt to boost celecoxib activity, a lymph-targeted celecoxib prodrug (Cele-Pro) mixed in HFD feed for 7–8 weeks (Fig. 5a). Cele-Pro consists of celecoxib linked to a glyceride backbone at the *sn*-2 position via a self-immolative linker (Fig. 5b). We previously showed that prodrugs with similar structures incorporate into dietary TG-absorption pathways, enhancing drug transport into mesenteric lymph[46,47]. Here we hypothesized that, by enhancing lymphatic transport, beneficial effects of celecoxib could be magnified, allowing for similar or improved effects at a lower dose. Consistent with previous studies, total celecoxib uptake into mesenteric lymph was increased more than tenfold when administered as Cele-Pro (Fig. 5c). In the treatment study, mice were administered a 3.5-fold lower dose of celecoxib in the form of Cele-Pro compared to that of the parent celecoxib. Parent celecoxib was administered at essentially the same dose (29 mg per kg per day) as that given in the prevention study (Fig. 4e–n). This strategy was employed to ensure

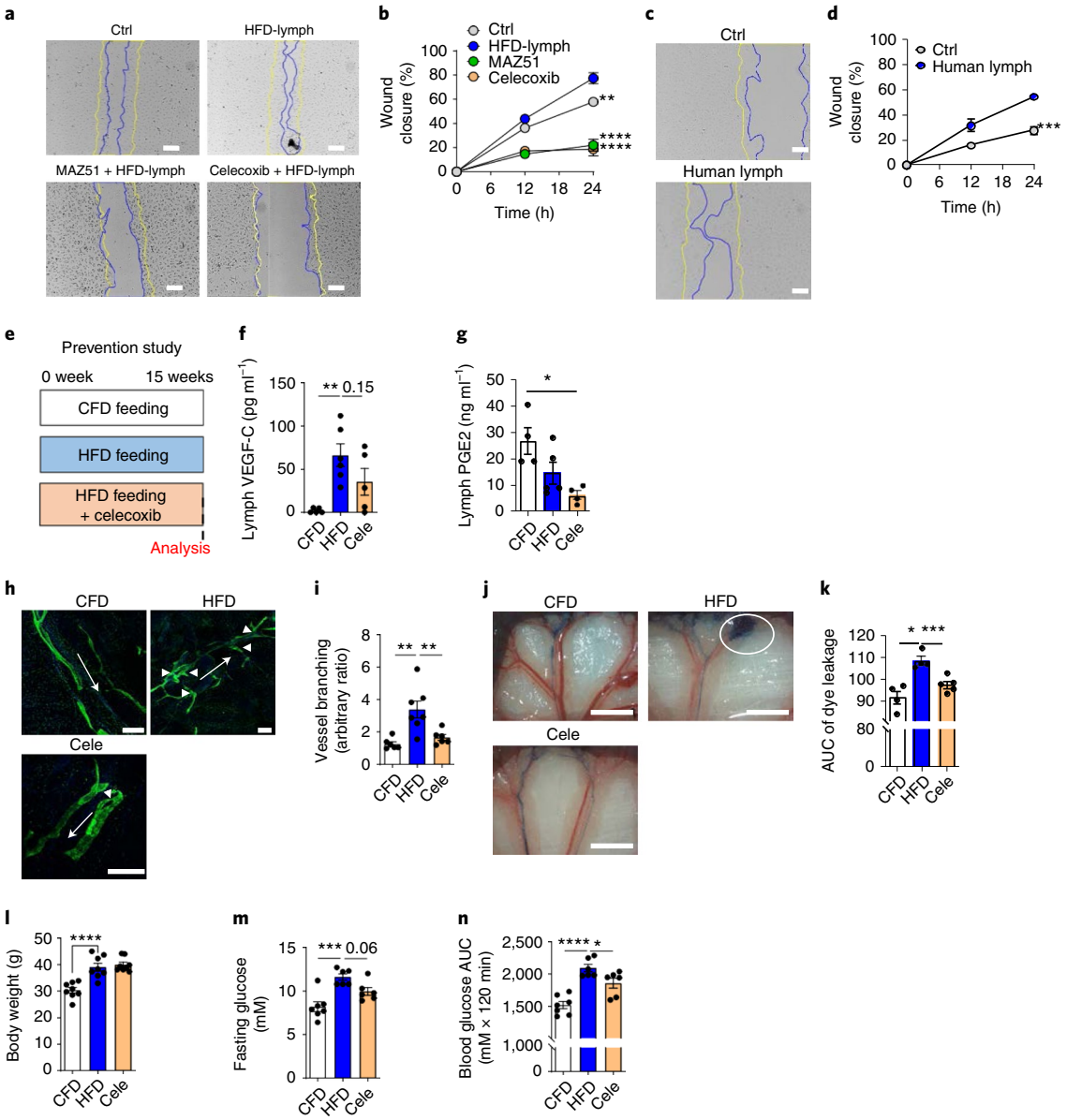


**Fig. 4 | COX-2–PGE2 and VEGF-C–VEGFR3 signalling regulate HFD-associated mesenteric lymphatic dysfunction and glucose intolerance.** Representative images of LEC wound closure (yellow, scratch at 0 h; blue, scratch at 24 h) (**a**,**c**) and quantification of LEC wound closure over time on incubation (**b**,**d**) with control medium (ctrl) or 2% (vol/vol) HFD-lymph from mice with or without MAZ51 or celecoxib (**a**,**b**) or 2% fed human lymph (**c**,**d**). Scale bar, 100 µm. Mean ± s.e.m. of $n = 11$, 9, 6 or 5 for $N = 4$ independent studies (**b**) and $n = 4$ or 5 for $N = 2$ independent experiments (**d**). **e**, Timeline for the celecoxib prevention study. **f**,**g**, VEGF-C and PGE2 concentration in lymph after 15 weeks of feeding the CFD, HFD or HFD with celecoxib (cele). Mean ± s.e.m. for $n = 6$, 7 or 6 mice (VEGF-C) and $n = 4$, 5 or 4 mice (PGE2). Representative immunofluorescence images (LYVE1 (green), Hoechst (blue)) (**h**) and quantification of mesenteric lymphatic vessel branching in VAT (**i**). Scale bar, 500 µm. Mean ± s.e.m. for $n = 6$, 7 or 6 mice. **j**, Representative images of Evans blue lymphangiography with a white circle showing lymph leakage sites. Scale bar, 5 mm. **k**, Quantification (AUC) of lymph leakage into VAT. Mean ± s.e.m. for $n = 4$, 4 or 5 mice. **l**, Body weight after 15 weeks of being fed the CFD or HFD with or without celecoxib. Mean ± s.e.m., $n = 8$, 8 or 8 mice. **m**, Fasting blood glucose. Mean ± s.e.m., $n = 7$, 6 or 6 mice. **n**, Blood glucose AUC from 0 to 120 min after the oral glucose tolerance test (OGTT). Mean ± s.e.m., $n = 7$, 6 or 6 mice. Statistical differences are from one-way ANOVA, $^{*}P < 0.05$, $^{**}P < 0.01$, $^{***}P < 0.005$ or $^{****}P < 0.001$. *P* values and details of statistical testing are provided as source data.

that plasma levels of celecoxib were lower after administration of Cele-Pro (Extended Data Fig. 6); and therefore that treatment benefits from Cele-Pro could be ascribed to lymph-specific effects.

Unlike in the prevention study, celecoxib did not reverse mesenteric lymphatic branching and lymph leakage in the treatment study, which is likely related to commencing treatment after disease has progressed. By contrast, treatment with a 3.5-fold lower dose of lymph-targeted Cele-Pro effectively reversed HFD-induced mesenteric lymphatic branching and lymph leakage into VAT to a level similar to that in mice fed the CFD (Fig. 5d–g). Consistent with its superior effect on lymphatic branching and leakage, only Cele-Pro (but not celecoxib) could completely abolish lymph VEGF-C, although both celecoxib and Cele-Pro reduced lymph PGE2 levels (Fig. 5h,i). This further supports the hypothesis that COX-2 and VEGF-C signalling promote mesenteric lymphatic branching and lymph leakage in obesity.

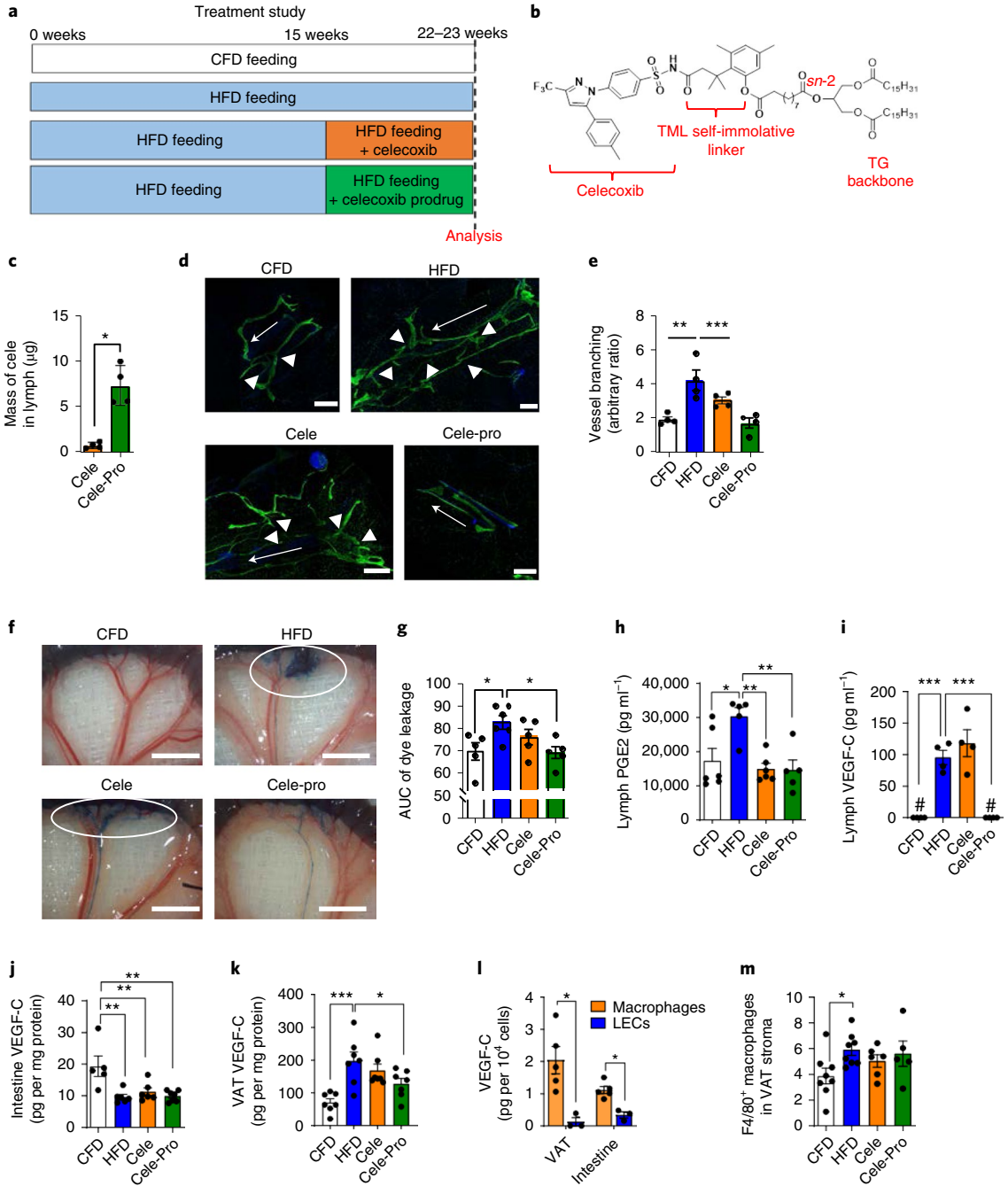


**Fig. 5 | Lymph-targeted COX-2 inhibition reverses HFD-induced mesenteric lymphatic branching and leakage by reducing local VEGF-C release.** **a**, Timeline of the celecoxib and lymph-targeted celecoxib prodrug (Cele-Pro) treatment study. **b**, Structure of the prodrug with celecoxib linked at the *sn*-2 position of 1,3-dipalmitin by an acyl spacer and a trimethyl lock (TML) self-immolative group. **c**, Total mass of celecoxib recovered in mesenteric lymph (in free or esterified form) over 6 h after intestinal administration of 0.18 mg celecoxib or Cele-Pro in a lipid-based formulation. Mean ± s.d., $n = 4$ and 4 mice. **d**, Lymphatic vessels in VAT (LYVE1 (green), Hoechst (blue)). Scale bars, 500 µm. **e**, Quantification of lymphatic vessel branching in VAT. Mean ± s.e.m., $n = 4$ mice for all groups. **f**, Representative images of Evans blue lymphangiography. White circles show sites of lymph leakage. Scale bar, 5 mm. **g**, Quantification (AUC) of lymph leakage into VAT. Mean ± s.e.m., $n = 5$, 6, 5 or 5 mice. **h**,**i**, PGE2 and VEGF-C concentrations in mesenteric lymph. Mean ± s.e.m., $n = 6$, 5, 6 or 6 mice (PGE2) and $n = 4$ mice for all groups (VEGF-C). The # symbol indicates below the limit of quantification. VEGF-C concentration in the intestine (mean ± s.e.m., $n = 5$, 7, or 7 mice) (**j**), VAT (mean ± s.e.m., $n = 5$, 7, 6 or 7 mice) (**k**), sorted macrophages and LECs from VAT and intestines of mice fed the HFD (mean ± s.e.m., $n = 5$, 3, 5 or 3 mice) (**l**) and percentage of macrophages ($CD45^+F4/80^+$) in VAT stromal cells (mean ± s.e.m., $n = 8$, 7, 6 or 5 mice) from mice fed the CFD or HFD for 23 weeks or mice fed the HFD for 23 weeks and treated with celecoxib or Cele-Pro from weeks 15 to 23 (**m**). Statistical differences are from two-tailed Mann–Whitney tests (**c**,**l**) or one-way ANOVA (**e**–**k**,**m**), $^*P < 0.05$, $^{**}P < 0.01$ or $^{***}P < 0.005$. *P* values and details of statistical testing are provided as source data.

Further, prostaglandins in addition to PGE2, for example, PGI2 and 6-keto-PGF1α, showed a significantly lower abundance in lymph and did not alter in concentration with HFD feeding or treatment (Extended Data Fig. 7a,b), suggesting that PGE2 was the major prostaglandin regulated in the COX-2 and VEGF-C signalling pathway.

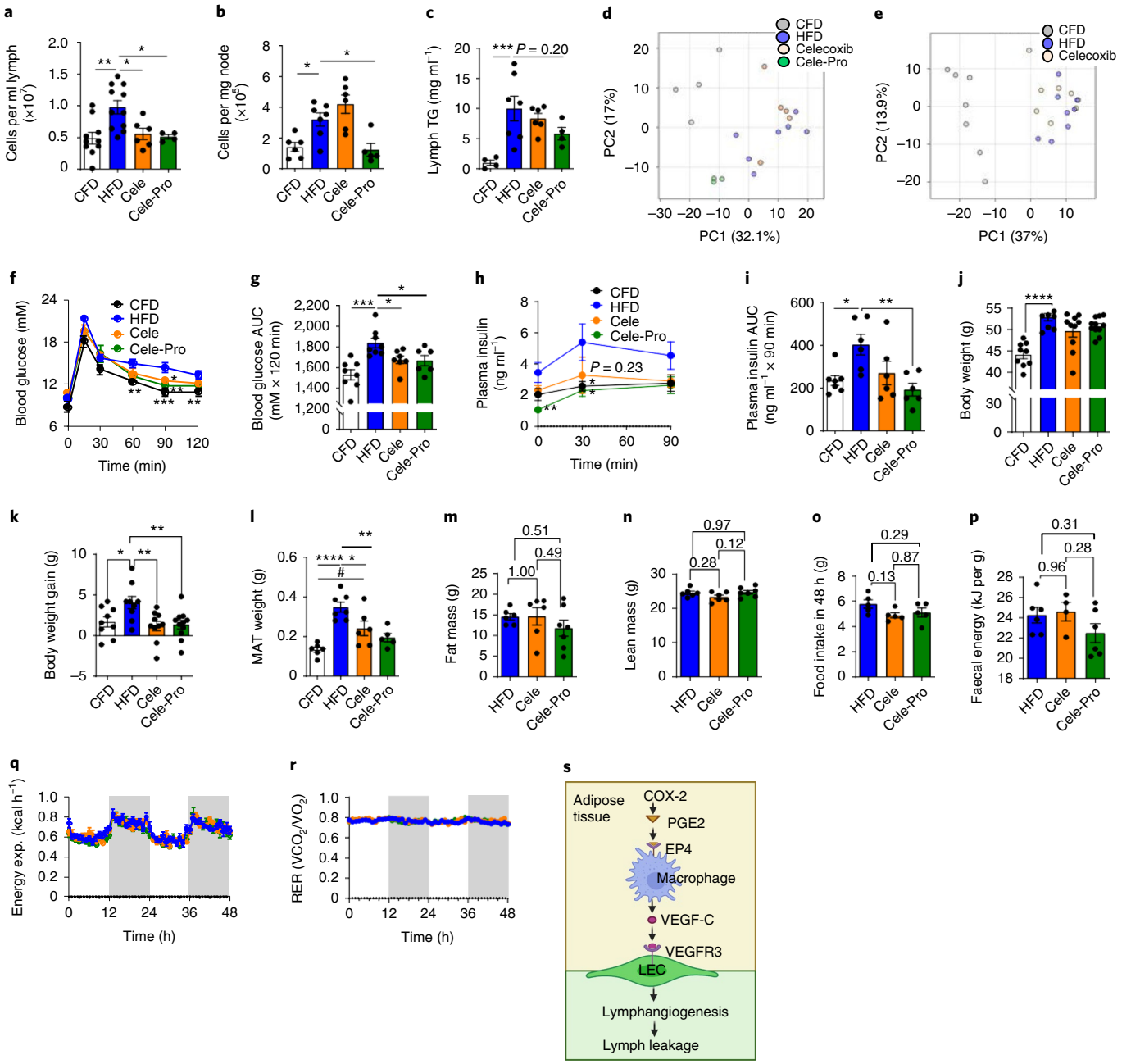


**Fig. 6 | Lymph-targeted COX-2 inhibition reverses insulin resistance through restoration of mesenteric lymphatic function, not modification of systemic metabolic function.** Data except those in **e** are for weeks 22–23 of the celecoxib and celecoxib prodrug (Cele-Pro) treatment study as shown in Fig. 5a. **a**,**b**, Total immune cells in mesenteric lymph fluid or nodes. Mean ± s.e.m., $n = 10$, 11, 6 or 5 mice (**a**) and $n = 6$, 7, 6 or 5 mice (**b**). **c**, TG concentrations in mesenteric lymph. Mean ± s.e.m., $n = 4$, 7, 6 or 4 mice. **d**,**e**, Unsupervised principal-component (PC) analysis of >500 annotated lipid metabolites in lymph from the treatment (Fig. 5a, timeline) or prevention (Fig. 4e, timeline) study. $n = 4$ (CFD), 7 (HFD), 5 (celecoxib) or 3 (Cele-Pro) mice (**d**) or $n = 7$ (CFD), 8 (HFD) or 8 (celecoxib) mice (**e**). **f**, Blood glucose over time after the OGTT. Mean ± s.e.m., $n = 8$, 8, 7 or 6 mice. **g**, AUC of blood glucose from 0 to 120 min after the OGTT. Mean ± s.e.m., $n = 8$, 8, 7 or 6 mice. **h**, Plasma insulin over time during the OGTT. Mean ± s.e.m., $n = 8$, 8, 6 or 7 mice (except $n = 9$ mice for CFD and HFD at 0 min and $n = 6$ or 8 mice for Cele-Pro at 30 min or 60 min). **i**, AUC of plasma insulin from 0 to 90 min after the OGTT. Mean ± s.e.m., $n = 7$, 6, 6 or 6 mice. Mice with missing samples were excluded from the AUC calculation. **j**, Body weight. Mean ± s.e.m., $n = 9$, 9, 10 or 11 mice. **k**, Weight gain of mice from the start of treatments. Mean ± s.e.m., $n = 9$, 9, 10 or 11 mice. **l**, Mesenteric adipose tissue (MAT) weight. Mean ± s.e.m., $n = 6$, 7, 6 or 5 mice. **m**, Total fat mass. Mean ± s.e.m., $n = 6$, 6 or 7 mice. **n**, Total lean mass. Mean ± s.e.m., $n = 6$, 6 or 7 mice. **o**, Food intake. Mean ± s.e.m., $n = 5$, 5 or 5 mice. **p**, Faecal energy. Mean ± s.e.m., $n = 6$, 4 or 6 mice. **q**, Energy expenditure (exp.). Mean ± s.e.m., $n = 6$, 6 or 7 mice. **r**, Respiratory exchange ratio (RER). Mean ± s.e.m., $n = 6$, 6 or 7 mice. **s**, Proposed mechanism of COX-2–PGE2–VEGF-C–VEGFR3 signalling in VAT that promotes lymphangiogenesis and lymph leakage. Statistical differences are from one-way ANOVA; statistics were compared to the HFD group except for those annotated with # ($^*P < 0.05$), which indicates statistics compared to the CFD group. $^*P < 0.05$, $^{**}P < 0.01$, $^{***}P < 0.005$ or $^{****}P < 0.001$. *P* values and details of statistical testing are provided as source data.

Next, we determined the source of VEGF-C that promotes mesenteric lymphatic branching and lymph leakage into VAT. VEGF-C in mesenteric lymph could be sourced from the intestine or VAT via direct drainage of these tissues or from blood via extravasation. However, plasma from mice fed the HFD contained only threefold higher VEGF-C levels than that from mice fed the

CFD (Extended Data Fig. 4d), suggested that systemic VEGF-C is unlikely to promote lymphatic vessel growth via access to the mesentery. Comparing VAT and the intestine, we found that the VEGF-C concentration was higher in VAT and increased significantly in VAT but not in the intestine with HFD feeding (Fig. 5i–k). Further, lymph-targeted Cele-Pro normalized VEGF-C concentrations in VAT and lymph to levels similar to those in mice fed the CFD, suggesting that VEGF-C in VAT and lymph promotes mesenteric lymphatic dysfunction and that Cele-Pro restores lymphatic function by normalising local VEGF-C levels. Within VAT and the intestine of mice fed the HFD, the concentration of VEGF-C was significantly higher in sorted macrophages than that in LECs (Fig. 5l), suggesting that macrophages are a major source of increased VEGF-C levels in VAT of mice fed the HFD. We further examined whether restoration of lymphatic function could be the result of a reduction in local macrophages. Neither celecoxib nor Cele-Pro reduced the HFD-induced increase in VAT stromal macrophages ($CD45^+F4/80^+$) (Fig. 5m), suggesting that Cele-Pro reduced lymphatic branching and leakage by reducing local VEGF-C release in VAT and not by reducing macrophages in VAT.

**Restoration of mesenteric lymphatic function reverses insulin resistance.** Next, we determined whether lymph-targeted COX-2 inhibition alters immune cells and lipid metabolites in mesenteric lymph and/or lymph nodes that regulate inflammation, metabolism and insulin resistance[48–50]. Both celecoxib and Cele-Pro treatments reduced immune cell numbers in the mesenteric lymph, but only Cele-Pro successfully reduced immune cell numbers in mesenteric lymph nodes to levels similar to those in mice fed the CFD, although the proportion of different types of immune cells did not change across groups (Fig. 6a,b and Extended Data Fig. 5g,h). Cele-Pro (but not celecoxib) treatment also significantly increased total FFA and decreased cholesterol levels (Extended Data Fig. 7c,d) in mesenteric lymph, whereas total lymph concentrations of TG (Fig. 6c), phospholipid and glucose (Extended Data Fig. 7e,f) were not significantly different across groups, indicating no significant changes in TG transport in lymph, suggesting that lacteal function was preserved. Both celecoxib and Cele-Pro reduced PGE2 in lymph; but, remarkably, lipidomic analysis of mesenteric lymph showed a shift in lymph lipid metabolites from an HFD-like profile toward a more CFD-like profile after Cele-Pro treatment (Fig. 6d and Extended Data Fig. 7g,h) but not after the celecoxib treatment or prevention regime in mice fed the HFD (Fig. 6d,e). In general, a range of sphingolipids (including ceramides), sterols and phospholipids (Extended Data Fig. 7g,h) were significantly increased in HFD-lymph compared to those from CFD-lymph, consistent with previously identified roles of ceramides and sphingomyelins in promoting insulin resistance[49,51]. Leakage of these lipids from lymph into adipose tissue may thus be a driver of local changes in metabolism. Another potential contributor is increased PGE2 levels in lymph (Fig. 5h); however, an EP4 antagonist did not significantly improve $^{14}$C-2DG uptake into adipocytes treated with HFD-lymph (Extended Data Fig. 4b,c).

Cele-Pro thus restored VAT lymphatic function, normalized pro-lymphangiogenic VEGF-C levels, reduced HFD-induced immune cell accumulation and reprogrammed lymph lipid metabolites. Importantly, lymph-targeted Cele-Pro improved systemic glycaemic control after an oral glucose challenge and reduced both fasting hyperinsulinaemia and glucose-stimulated insulin to levels that were indistinguishable from those in mice fed the CFD (Fig. 6f–i). By contrast, while celecoxib improved oral glucose tolerance, it did not significantly improve HFD-induced hyperinsulinaemia (Fig. 6f–i). More remarkably, when we examined oral glucose tolerance and hyperinsulinaemia after administration of a range of doses of celecoxib and Cele-Pro from weeks 15 to 23 of HFD feeding, we showed that Cele-Pro could restore normoglycaemia and normoinsulinaemia at approximately tenfold lower doses than celecoxib (Extended Data Fig. 8), supporting the suggestion that local regulation of mesenteric lymphatic function improves systemic glycaemic control. Further, while both celecoxib and Cele-Pro reduced HFD-induced body weight gain and increases in mesenteric adipose tissue mass without altering total body weight or fat/lean mass (Fig. 6j–n), only Cele-Pro reduced mesenteric adipose tissue mass to a level that was not statistically different than that at CFD baseline (Fig. 6l). Lymph-targeted Cele-Pro thus had overall superior beneficial effects on lymphatic function and composition, body weight gain, visceral adiposity and glycaemic control compared to systemic COX-2 inhibition with celecoxib, despite the fact that Cele-Pro was administered at doses up to tenfold lower than those for celecoxib.

To further confirm that the improvement in glycaemic control by Cele-Pro was a result of restoration of mesenteric lymphatic function rather than effects on systemic metabolism, we also examined food intake, faecal energy excretion, energy expenditure and the respiratory exchange ratio. All were unchanged after treatment of mice fed the HFD with either celecoxib or Cele-Pro (Fig. 6o–r), suggesting that the treatment benefit of Cele-Pro occurs through targeting local lymphatics rather than modifying systemic metabolism.

## Discussion

Our data reveal that there is extensive remodelling of mesenteric lymphatics in humans with obesity and mice fed the HFD. Mesenteric lymphatic vessels become highly branched and 'leaky', resulting in leakage of HFD-modified lymph into VAT, which promotes VAT accumulation and metabolic changes that promote insulin resistance. We demonstrate that mesenteric lymphatic dysfunction is mediated by activation of COX-2–PGE2 and VEGF-C–VEGFR3 signalling and that lymph-targeted COX-2 inhibition effectively reverses mesenteric lymphatic dysfunction, blocks weight gain, restores glycaemic control and reduces hyperinsulinaemia in obese mice. We thus present mesenteric lymphatic dysfunction as a cause of and therapeutic target for obesity and insulin resistance.

Structural changes to lymphatic vasculature have been described in peripheral tissues in obesity[15–21]. Here we comprehensively profile changes to lymphatics in the small intestine and VAT of obese mice fed the HFD and humans with obesity. Importantly, VAT is the adipose tissue depot most correlated with metabolic disease[28–30]. Within VAT, we found that mesenteric lymphatic vessels become highly branched in humans with obesity and obese mice fed the HFD compared to those in lean humans and mice fed the CFD. We also found that mesenteric lymph fluid leaks from lymphatic vessels around vessel branch points in mice fed the HFD, suggesting that lymph leakage is a result of dysfunctional lymphangiogenesis. Previous data from Scallan et al. showed increases in mesenteric lymphatic vessel permeability in diabetic *db*/*db* mice[32]. By contrast, we found that mesenteric lymphatic branching and lymph leakage were not increased in diabetic *db*/*db* mice. This may have resulted from differences in methodology, as, in the previous study, permeability was measured by ex vivo perfusion of an isolated lymphatic vessel[32], whereas we measured lymph leakage by lymphangiography in live mice. Importantly, our data suggest that the diabetic *db*/*db* model does not recapitulate the mesenteric lymphatic dysfunction observed in humans in whom obesity is usually driven by diet.

Further, increases in lymphangiogenesis and lymph leakage in VAT in the current study also contrast with those reported for lymphatic vessels in peripheral tissues of rodents[15–18] and humans[19–21] with obesity and/or diabetes in which lymphatic vessel density, contractility and transport properties are decreased. The changes are, however, consistent with the findings of Harvey et al. in *Prox1*$^+$ or *Prox1*$^-$ mice in which mesenteric lymph leakage was associated with the development of obesity[25]. Different compositional and structural alterations of mesenteric lymphatics compared to peripheral lymphatics in HFD-induced obesity likely reflect their different

physiological roles. Mesenteric lymphatics receive high concentrations of lipid metabolites, gut hormones, antigens, immune cells, microbial products and other factors from the intestine and VAT, whereas peripheral lymphatics drain factors such as macromolecules and immune cells from tissues such as the skin, muscle and SAT[3,4]. HFDs amplify differences in mesenteric lymph composition[52–54]. Our data further show that pro-inflammatory immune cell numbers and levels of pro-lymphangiogenic factors and long-chain lipid metabolites are significantly increased in mesenteric lymph in obesity. Compositional and structural changes to mesenteric lymphatics also appear to be driven by diet, as diabetic *db*/*db* mice fed a CFD did not develop mesenteric lymphatic changes despite being more obese than C57BL/6 mice fed the HFD. Compositional differences in mesenteric lymph compared to peripheral lymph may thus lead to site-specific lymphangiogenesis in VAT but not in SAT. This showcases the remarkable plasticity and heterogeneity of lymphatic structure and function, even at notionally similar adipose tissue depots (for example, SAT versus VAT), which are both shaped by and control their local tissue microenvironment[4].

The most important aspect of the current work is the finding that mesenteric lymph leakage in mice fed the HFD promotes accumulation of VAT and insulin resistance in VAT, which, when reversed with the lymph-targeted prodrug of the COX-2 inhibitor celecoxib, significantly reduces visceral adiposity and improves glycaemic control. Adipose tissue accumulation around sites of lymph leakage has been observed previously[25,55] but primarily in transgenic mice with dysfunctional lymphatics and in non-obesity settings. Our studies here suggest that VAT metabolism is directly regulated by local lymphatic function, as insulin resistance in VAT was not homogeneous but most significant at sites around leaky lymphatics in obese mice. These findings could explain why the expansion of VAT, which surrounds mesenteric lymphatics, leads to greater metabolic and inflammatory changes and insulin resistance than SAT expansion[28–30,56]. We further show that HFD-lymph promotes changes to adipocyte function including increases in adipogenesis, lipid accumulation and lipolysis. These changes are consistent with pathological changes to VAT in vivo that promote lipid deposition and inflammation in VAT, muscle and liver and thus promote systemic insulin resistance[28–30]. Metabolism may also be impacted by the change in lipid-deposition profiles in tissues where there is significant lymph leakage to VAT. Recent studies have shown that the lipid fraction but not the protein fraction in lymph promotes adipocyte differentiation and lipid storage and have suggested that this is mediated by FFAs in lymph[37,57]. However, in our study, FFA levels in HFD-lymph were not elevated above those in CFD-lymph. Instead, we found that HFD-lymph is enriched with lipids such as long-chain (C14–C22) ceramides and sphingomyelins that are linked to obesity and insulin resistance[49,51]. The leakage of lymph lipid metabolites to the surrounding VAT may thus contribute to local insulin resistance.

Concomitant with modulation of adipose tissue metabolism, we show that HFD-lymph contains >100-fold higher levels of pro-lymphangiogenic VEGF-C than CFD-lymph and that this promotes mesenteric lymphatic vessel growth. Thus, HFD-lymph from mice and fed lymph from a human promoted LEC closure of a scratch wound in vitro. The increase in VEGF-C in HFD-lymph that promoted lymphangiogenesis appeared to be sourced from VAT (rather than the intestine or blood) and to be released by macrophages in VAT. We hypothesized that PGE2 synthesized by COX-2 regulates VEGF-C release from macrophages and thus lymphatic vessel growth in a manner similar to that in other inflammatory conditions. We thus completed treatment studies with the COX-2 inhibitor celecoxib and a lymph-targeted glyceride prodrug, Cele-Pro, that we developed to concentrate celecoxib at the site of lymph leakage to VAT[46,47]. Lymph-targeted Cele-Pro reduced VEGF-C levels in VAT and mesenteric lymph (without changing the percentage of macrophages in VAT stroma) and reversed mesenteric lymphatic dysfunction in obese mice fed the HFD in vivo, supporting the suggestion that activation of COX-2–PGE2 and VEGF-C–VEGFR3 pathways promotes mesenteric lymphatic branching and leakage (see mechanism in Fig. 6s). Altered nitric oxide signalling and increases in lymph FFA levels were previously reported to promote lymphatic vessel hyperpermeability in obesity and/or diabetes[24,32,37,57]. By contrast, in the current study, FFA levels in mesenteric lymph were not altered with HFD feeding and were in fact increased by treatment with lymph-targeted Cele-Pro, and this occurred in tandem with reversed lymphatic leakage.

Treatment with the lymph-targeted Cele-Pro compared to treatment with non-targeted celecoxib also more effectively reversed mesenteric lymphatic vessel branching and lymph leakage and altered the lipid metabolic profile of mesenteric lymph, rendering it more 'CFD-like' than 'HFD-like'. This targeted reversal of mesenteric lymphatic dysfunction by treatment with the celecoxib prodrug led to effective reversal of visceral adiposity, glucose intolerance and hyperinsulinaemia in mice fed the HFD. Both the switch in the lymph lipid metabolites to a 'healthier' profile and the reduction in lymph leakage to VAT are expected to contribute to restoration of local VAT metabolism and thus improved glycaemic control on treatment with the prodrug. Through site-specific delivery to lymph, Cele-Pro increases the efficacy and therapeutic window of celecoxib. We thus propose that mesenteric lymph-targeted treatments, including lymph-specific COX-2 inhibition, are a potential strategy to combat obesity-associated metabolic disease and warrant further evaluation.

In summary, we demonstrate a mesenteric lymphatic vessel-centred pathophysiological mechanism that contributes to visceral obesity and insulin resistance. We also demonstrate the potential to treat obesity and insulin resistance through normalisation of mesenteric lymphatic function. Future studies will explore whether obesity-associated impairments to mesenteric lymphatic function (that is, fluid clearance, lipid metabolism and immunity) impart susceptibility to other chronic diseases.

## Methods

**Antibodies and chemicals.** All chemicals and reagents are listed in Supplementary Table 1.

**Human studies.** Human studies were approved by the New Zealand Health and Disability Ethics Committees and conducted according to ethical guidelines, and informed consent was obtained from patients. Patients received no payment. Thoracic lymph was collected from a male patient with obesity (92 kg, BMI > 30) with a catheter inserted into the thoracic duct during Ivor Lewis oesophagogastrectomy (as reported in ref. [58]). The patient received only intravenous fluid during lymph sampling. Mesenteric adipose tissue was collected from patients who were obese or lean (selection criteria are in Supplementary Table 2) during Roux-en-Y procedures. Images were from two patients with obesity (patient 1, female, 31 years old; patient 2, female, 41 years old) and three lean patients (patient 1, male, 70 years old; patient 2, female, 49 years old; patient 3, female, 75 years old).

**Lymphatic analysis in human tissue.** Mesenteric adipose tissue was cleared using the Adipo-Clear method[59] with modifications for light-sheet imaging. Samples were dehydrated in 20%, 40%, 60% and then 80% methanol in B1N buffer (0.5% Triton X-100, 0.3 M glycine, pH 7) and 100% methanol for 30 min each. Samples were delipidated with 100% dichloromethane for 45 min twice and then washed with 100% methanol for 30 min and then with 80%, 60%, 40% and 20% methanol in B1N buffer for 30 min for each step. Samples were washed with B1N buffer for 30 min, followed by permeabilisation in 0.5% Triton X-100, 0.05% Tween-20 and 2 IU $ml^{-1}$ heparin in PBS (PTwH buffer) for 1 h. Tissues were bleached in 10% $H_2O_2$ at 55 °C for 20 min and washed with B1N buffer for 30 min. Samples were then incubated with 1 µg $ml^{-1}$ anti-human podoplanin antibody in PTwH buffer for 5 d at 4 °C. Samples were then washed and incubated with 2 µg $ml^{-1}$ donkey anti-sheep secondary antibody conjugated with Alexa 647 in PTwH buffer overnight at 4 °C. Stained tissues were dehydrated in 25%, 50% and 75% methanol in water and then in 100% methanol and washed with 100% dichloromethane, followed by clearing in dibenzyl ether for approximately 24 h.

Samples were imaged on a light-sheet microscope (UltraMicroscope II, LaVision BioTec) equipped with an MVPLAPO ×2 lens with a numerical aperture of 0.5 (Olympus) and an LV OM DCC20 dipping cap with a working distance of 5.7 mm (LaVision BioTec) mounted on a variable zoom body MVX10 (Olympus). An sCMOS camera (2,560 × 2,160 pixels) (Andor Neo) and ImspectorPro software (LaVision BioTec) was used for image acquisition. For acquisitions, a sequential double-side illumination followed by a merge of left and right light-sheet views using an Imspector inbuilt contrast method was used. Samples were mounted using custom sample holders and immersed in a quartz imaging cuvette filled with ethyl cinnamate with a refractive index of 1.558. Samples were scanned using a diode 639-nm laser and a 680/30-nm emission filter. Light-sheet thickness was 5 µm. For 3D acquisitions, the *z*-stack step size was 5–8 µm, and the zoom factor was 0.8–1.6×.

Whole-tissue images were generated using Imaris x64 software (version 9.3.1, Bitplane). The 'volume render' function was used for 3D reconstruction. Optical slices were obtained using the 'orthoslicer' tool. Lymphatic vessel tortuosity ratios were calculated as described in Supplementary Fig. 1.

**Animal studies.** Animal work was approved by the Monash Institute of Pharmaceutical Sciences Animal Ethics Committee and conducted according to Australian National Health and Medical Research Council guidelines for the care and use of animals in research. Male Sprague Dawley rats or C57BL6/J mice (6–7 weeks old) were randomized and housed in groups of two to five in a 12-h light–12-h dark cycle at 22–25 °C and with 35–37% humidity. Animals were fed a semi-purified normal chow diet (CFD, 8.5% (wt/wt) fat; 102119, Barastoc) or the HFD (36% (wt/wt) fat; SF15-107, Specialty Feeds) for 6–32 weeks for mice and 6–9 weeks for rats.

In mice, a prevention study and a treatment study were conducted with timelines as shown in Figs. 4e and 5a. Celecoxib and celecoxib prodrug (Cele-Pro) were incorporated into HFD feed at a dose of ~29 mg per kg per day (based on mean food intake). Celecoxib prodrug synthesis and NMR spectra are shown in Supplementary Fig. 6.

**Lymphatic-structure analysis in mice.** Intestinal tissue (cut into 1.5-cm sections) was taken from the mouse duodenum, ~2.5 cm past the stomach, as dietary lipids are predominantly absorbed in this region. Whole-mount mesenteric adipose tissue was cut in ~3 × 3 × 2-mm pieces. FALCs were identified by intraperitoneal injection of 100-nm FluoSphere Carboxylate-Modified Nanospheres, yellow–green (505/515A) and collected under a Zeiss Stemi 2000-CS surgical microscope (2.5× magnification) with a fluorescence adaptor (excitation/emission, 440–560 nm/500 nm) (Nightsea).

After fixation and blocking, tissues were incubated with primary antibodies (Supplementary Table 3) for 3–4 d at 4 °C and then overnight with secondary antibodies (Supplementary Table 3). Some samples were incubated with 5 µg ml$^{-1}$ BODIPY FA C16 fatty acid and/or 1:200 NucBlue Live ReadyProbes Reagent. Sequential primary antibody staining was achieved through an additional blocking step with 10% rat serum (Sigma) followed by the addition of 10 µg ml$^{-1}$ goat anti-rat Fab fragments. After staining intestinal tissue, a 0.5-mm segment, containing ~10–15 villi, was isolated for imaging. All stained tissues were mounted on slides with fluorescent mounting medium.

Tissues were imaged using a Leica SP8 inverted confocal microscope with a ×20 Plan Apo CS2 0.75-NA objective controlled by LAS AF (version 3.5.5) image-acquisition and -processing software (Leica). Excitation/emission wavelengths were 405 nm/490 nm for Alexa 405, 495 nm/550 nm for Alexa 488, 550 nm/600 nm for Alexa 568 and 600 nm/700 nm for Alexa 647. The image format was 512 × 512 pixels, and scan frequency was 400 Hz. *z* stacks had a step size of 5.5–6 µm. Images were analysed using the Fiji distribution of ImageJ[60].

In intestinal tissue, villi and lacteal width were quantified from the average of three straight lines drawn manually at the base, midpoint and near the tip using the drawing tool in ImageJ. To measure villi and lacteal length, a single line was drawn manually from tip to base. In adipose tissue, number and average size of adipocytes was counted from the number of lipid droplets and the ratio of BODIPY + area divided by the number of adipocytes. In adipose tissue, a lymphatic vessel-branching ratio was calculated as shown in Supplementary Fig. 3.

**Quantification of lymph leakage in mice.** Mesenteric lymphatic vessel leakage was measured using a new Evans blue dye lymphangiography method. The small intestine was externalized through an abdominal incision and moistened with warm PBS. A 4–5-cm segment of duodenum or jejunum containing a Peyer's patch was isolated. Next, 5 µl 10% Evans blue dye was injected into the upper layer of the Peyer's patch. Drainage of Evans blue dye through mesenteric lymphatic vessels and leakage into surrounding VAT was recorded at 2, 5, 10, 20 and 30 min after injection (Supplementary Fig. 4). Images were captured using a Zeiss Stemi 2000-CS surgical microscope mounted with an Axiocam ERc 5s camera and AxioVision software with 2.5× magnification (Zeiss).

The red channel (560 nm) of the image was used for quantification using Fiji software. At the four to five most leaky sites (10-min time point), a straight line (approximately ten pixels) was drawn across the lymphatic vessel and surrounding adipose tissue using the straight-line tool in Fiji. Dye intensity was measured from the centre of the lymphatic vessel outward to adipose tissue. Data of dye intensity were extracted and transformed to standardize against the maximum signal intensity. This resulted in a bell-shaped intensity distribution in which the greatest dye intensity was in the lymphatic vessel.

**Mesenteric lymph collection and impact on adipocytes.** The efferent mesenteric lymphatic duct was cannulated in rats[61] and mice[62] as described previously. Lymph was collected for up to 4 h in non-fasted animals.

Fibroblasts (3T3-L1) (ATCC cell lines) were cultured to allow differentiation into pre-adipocytes and mature adipocytes, as described previously[63]. The 3T3-L1 cells were exposed to growth medium (control) or 2% (vol/vol) rat CFD-lymph or HFD-lymph in growth medium for 2–3 d, when either early fibroblasts (experiment 1) or mature adipocytes (experiment 2) were confluent as shown in Supplementary Fig. 5. Human subcutaneous pre-adipocytes (HMLEC-dLyAd from Lonza) were cultured and differentiated according to the manufacturer's instructions with modification of the differentiation medium. Briefly, pre-adipocytes were differentiated with medium that contained 0.25 mM 3-isobutyl-1-methylxantine, 1 µM dexamethasone, 10 µg ml$^{-1}$ insulin and 200 µM indomethacin. Mature adipocytes were exposed to growth medium (control) or 2% (vol/vol) rat HFD-lymph in growth medium for 2–3 d (experiment 1) as shown in Supplementary Fig. 5.

**Adipocyte marker mRNA expression.** At day 9 (Supplementary Fig. 5, experiment 1), adipocyte total RNA was isolated with QIAzol–chloroform extraction and isopropanol precipitation. DNA contamination was removed by digestion with DNase I (DNA-free removal kit, Invitrogen). First-strand cDNA was synthesized from RNA using the iScript cDNA Synthesis kit (Bio-Rad). Quantitative reverse-transcription–PCR assays were performed using a Bio-Rad Thermocycler 1000 (Bio-Rad) and TaqMan gene expression assays (Supplementary Table 4). mRNA expression was normalized to 18S rRNA expression using the $\Delta\Delta C_t$ method[64].

**Adipocyte morphology.** At day 11 (Supplementary Fig. 5, experiment 2), mature adipocytes were fixed and stained with 2 µg ml$^{-1}$ BODIPY 493/503 and Hoechst at 1:200 (vol/vol) for 10 min. Adipocyte morphology was assessed from images acquired using a Leica SP8 inverted confocal microscope (×63 oil-immersion objective, 1.5× magnification) controlled by LAS AF image software (Leica). Images were acquired as a 10–15-µm *z* stack with a step size of 0.5 µm and a line average of 2. Captured images were analysed using Fiji (ImageJ) software[60].

**Adipocyte lipolysis.** At day 11 (Supplementary Fig. 5, experiment 2), mature adipocytes were incubated in oxygenated Krebs buffer substituted with 8 mM glucose and 1% (wt/vol) BSA for 2 h in the presence or absence of 20 µM forskolin to stimulate lipolysis. The supernatant was collected for analysis of glycerol release (Free Glycerol Reagent kit, F6428, Sigma Aldrich).

**Adipocyte intracellular triglyceride accumulation.** At day 11 (Supplementary Fig. 5, experiment 2), mature adipocytes were lysed by passing them through a fine needle five times. TGs were extracted in 2:1 chloroform:methanol. The organic layer was dried and concentrated in 95% (vol/vol) ethanol in water. TG concentration was measured using a serum TG determination kit (TR0100, Sigma).

**Adipocyte glucose uptake.** At day 11 (Supplementary Fig. 5, experiment 2), mature adipocytes were incubated with oxygenated DMEM supplemented with 8 mM $^{14}$C-2DG, 2.5 mM sodium pyruvate and 1% (wt/vol) BSA with or without 10 nM insulin for 10 min at 37 °C. Next, adipocytes were incubated with or without EP4 antagonist (L-161,982) with 7.5 µM $^{14}$C-2DG (0.4 µCi ml$^{-1}$) in DMEM under the insulin-stimulated or basal condition. Cells were lysed and resuspended for scintillation counting (Packard Tri-Carb 2000CA Liquid Scintillation Analyzer (Packard)), followed by correction for adipocyte protein concentration (Pierce BCA protein-analysis kit, Thermo Scientific).

**Mesenteric adipose tissue glucose uptake.** Mesenteric adipose tissue (20–40 mg) was isolated from mice fed the CFD and HFD at leaky and non-leaky regions of lymphatic vessels, as assessed by Evans blue lymphangiography. Glucose uptake was estimated using the analogue $^{14}$C-2DG[65,66]. Adipose tissue was incubated at 37 °C with 5% $CO_2$ for 30 min in oxygenated DMEM containing 8 mM $^{14}$C-2DG, 2.5 mM sodium pyruvate and 1% (wt/vol) BSA. Next, adipose tissue was treated with 100 nM insulin in Krebs buffer supplemented with 8 mM $^{14}$C-2DG, 2.5 mM sodium pyruvate and 1% (wt/vol) BSA for 20 min, followed by incubation with 7.5 µM $^{14}$C-2DG (0.4 µCi ml$^{-1}$) in Krebs buffer[67], supplemented as before, for 20 min. Tissues were processed for scintillation counting and protein-content analysis as described for adipocytes.

**Flow cytometry.** Mesenteric lymph fluid (30–40 µl) was pelleted, washed and stained for flow cytometry. Lymph nodes were also collected, weighed and passed through a 70-µm cell mesh to obtain a single-cell suspension. Cells were stained with antibodies at the concentrations listed in Supplementary Table 5 in the dark at 4 °C for 20 min. For helper T cell analysis, an aliquot of the single-cell suspensions

was stimulated with 50 ng ml$^{-1}$ PMA and 1 µg ml$^{-1}$ ionomycin in 0.5% (vol/vol) FBS in RPMI 1640 medium for 3.5 h in the presence of Golgi Stop. After stimulation, cells were stained for surface markers, fixed and permeabilized using the Cytofix/Cytoperm kit, followed by intracellular cytokine staining (Supplementary Table 5) for 20 min. Cells were analysed using a BD FACSCanto II (BD Biosciences) and FlowJo software version 10 (Tree Star). All appropriate controls, including negative controls, compensation controls and fluorescence-minus-one controls, were applied. The gating strategy is shown in Supplementary Fig. 7.

**Isolation and sorting of cells.** Cells were isolated from mesenteric adipose tissue and small intestinal lamina propria as described previously[68,69]. Briefly, adipose tissue was removed, chopped and minced in digestion medium containing collagenase II (2–3 mg ml$^{-1}$) in 2% FBS in PBS and incubated for 35 min at 37 °C. Adipose tissue digest was filtered (100-µm cell strainer). For cell extraction from small intestinal lamina propria, tissue was washed, minced and digested in collagenase D (0.05 mg ml$^{-1}$), DNase I (0.5 mg ml$^{-1}$) and dispase II (3 mg ml$^{-1}$) for 15 min at 37 °C with agitation and filtered (70-µm filters). Filtered cells were washed and stained (Supplementary Table 5) for cell sorting. Macrophages (CD45$^+$CD11b$^+$F4/80$^+$) and LECs (CD45$^-$CD31$^-$LYVE1$^+$podoplanin$^+$) were sorted using a Beckman Coulter MoFlo Astrios cell sorter and pelleted for ELISA analysis. The gating strategy is shown in Supplementary Fig. 7.

**Enzyme-linked immunosorbent assays.** Samples were preserved at −20 °C until ELISAs were conducted. VEGF-C and prostaglandin concentrations were measured using kits (VEGF-C (CSB-E07361m), PGI2 (CSB-E13698m), 6-keto-prostaglandin F1α (CSB-E09422m), Cusabio Life Science; PGE2, ab133021, Abcam). Insulin concentration was measured using an ELISA kit (Crystal Chem). The dilution factor for insulin in plasma was 1:5.

**Lymph- and blood-composition analysis, including lipidomics.** Commercial kits were used to analyse TG (TR0100, Sigma), total cholesterol (A12216, Invitrogen) and FFA and phospholipid (HR Series NEFA-HR (2), 434-91795 and Phospholipid C kit, 997-01801 from Wako Pure Chemical Industries).

For lipidomic analysis, lipids were extracted from 50 µl mesenteric lymph using 200 µl $CHCl_3$:MeOH (1:3 (vol/vol)). Samples were mixed for 1 h at 4 °C and centrifuged at 16,000*g* for 10 min, and the extract was dried with nitrogen gas and reconstituted in 200 µl BuOH:MeOH:$H_2O$ (45:45:10, vol/vol). After sonicating in a bath with ice, samples were centrifuged for 10 min at 16,000*g*, and supernatants were transferred to vials. Samples (10 µl) were analysed using an untargeted lipidomic workflow as previously described[70]. LC–MS data were acquired on a Q Exactive Orbitrap mass spectrometer (Thermo Scientific) coupled with the Dionex UltiMate 3000 RS HPLC system (Thermo Scientific) and processed using IDEOM software[71]. Lipid identifications based on accurate mass within a mass tolerance of 3 ppm were deemed MSI level 3 (ref. [72]). Multivariate statistical analysis was performed using MetaboAnalyst[73].

**Lymphatic endothelial cell assays.** LECs from adult human skin (HMLEC-dLyAd) were from Lonza and propagated in EGM-2MV BulletKit medium (EBM; CC-3162, Lonza). Cells were seeded onto plates precoated with rat tail collagen type I (50 µg ml$^{-1}$) for 1 h at 37 °C. Once cells reached confluence, a scratch assay was performed to assess the impact of lymph fluid on LEC migration. LECs were starved in EBM containing 0.5% (wt/vol) FBS for 6 h to overnight. A scratch was made using a 200-µl pipette tip, and cells were incubated for up to 30 h in 0.5% FBS (wt/vol) in EBM medium with or without 2% lymph from mice fed the CFD or HFD or from the human patient with obesity. The VEGFR3 kinase inhibitor MAZ51 (5 µM), the EP4 antagonist (L-161,982) or the COX-2 inhibitor celecoxib (20 µM) were added during HFD-lymph treatment. Images were captured hourly using an Operetta high-content imaging system (PerkinElmer). Images acquired at 0, 12 and 24 h were analysed using Fiji (ImageJ) to determine the rate of closure of the scratched wound.

**Metabolic measurements in mice.** Across all studies, body mass was measured weekly. OGTTs were conducted as described previously[74] at 5, 14, 22 and/or 31 weeks after starting CFD or HFD feeding in mice. Blood glucose levels were measured using a one-touch glucometer (Accu-Chek Performa, Roche). Plasma was collected to measure insulin levels by ELISA.

Food intake was manually measured for mice singly housed for 48 h. Daily faecal caloric content was measured with an oxygen bomb calorimeter and calculated from total faecal mass. Mouse body composition was measured in a Minispec MRI body-composition analyser (Bruker). Whole-body energy expenditure was measured with a Comprehensive Laboratory Animal Monitoring System[75] (Promethion, Sable Systems). At the end of each experiment, adipose tissue depots were collected and weighed.

**Lymph and plasma pharmacokinetics of celecoxib and prodrug.** *Formulations.* For the lymphatic transport study, formulations contained 6.67 mg per kg celecoxib or prodrug, 133 mg per kg oleic acid and 73.3 mg per kg Tween-80 in 0.5 ml PBS (pH 7.4), emulsified by ultrasonication with a Misonix XL2020 ultrasonic processor (Misonix). For the plasma pharmacokinetic study, 29 mg per kg celecoxib or prodrug (equivalent of ~9 mg per kg celecoxib) was emulsified in a mixture of 0.3 ml oleic acid (Sigma Aldrich), cremophor RH40 (Sigma Aldrich) and ethanol (40:52.6:7.4 (wt/wt/wt)) in PBS.

*Study design.* For lymphatic transport, mesenteric lymph duct and duodenum were cannulated after a 3–4-h fast, as described previously[62]. Celecoxib or prodrug formulations were administered via intraduodenal infusion over 1 h, followed by rehydration. Lymph was collected hourly for up to 6 h. For plasma exposure, 0.3 ml celecoxib or prodrug lipid formulations were administered by oral gavage. Blood samples (100 µl) were collected at set time points, and plasma was separated.

*Preparation of lymph and plasma for HPLC–MS/MS analysis.* To measure celecoxib concentrations in lymph, 250 µl acetonitrile was added to 20-µl lymph samples. Samples were vortexed and centrifuged (4,500*g* for 5 min), and supernatants were used for HPLC–MS/MS. To determine the prodrug concentration in lymph, 5 µl of a 1 µg ml$^{-1}$ solution of internal standard (5,5-diethyl-1,3-diphenyl-2-iminobarbituric acid) was added to 20 µl lymph. In vitro hydrolysis was used to liberate celecoxib from the glyceride backbone to quantify total celecoxib derivatives. NaOH (140 µl, 0.5 M) in 1:1 (vol/vol) ethanol:water was added to 20 µl lymph and incubated at 60 °C for 20 min. HCl (70 µl, 1 M) was added to terminate hydrolysis. Samples were diluted 2.3-fold with 80% (vol/vol) acetonitrile and 0.1% (vol/vol) formic acid in water. Samples were vortexed and centrifuged (4,500*g* for 5 min), and supernatants were assayed by HPLC–MS/MS.

Celecoxib concentrations were measured in plasma, as only celecoxib liberated from prodrug was expected to be active. Briefly, 200 µl acetonitrile was added to 20 µl plasma and 5 µl of a 1 µg ml$^{-1}$ solution of internal standard (as described above) in acetonitrile. Samples were vortexed and centrifuged (4,500*g* for 5 min), and supernatants were assayed by HPLC–MS/MS.

*HPLC–MS/MS analysis of celecoxib and prodrug.* For HPLC–MS/MS analysis, we used a Shimadzu LCMS-8050 (Shimadzu Scientific Instruments), comprising a CBM-20A system controller, a DGU-20A5R solvent degasser, LC-30AD pumps, a SIL-30AC autosampler, a CTO-20AC column oven (40 °C) and a triple quadrupole MS with an electrospray ionisation interface. The desolvation line and heat block were at 250 °C and 400 °C. Interface and detector voltages were 4.0 kV and 2.3 kV. Nebulising and drying gas flow rates were 3 l min$^{-1}$ and 10 l min$^{-1}$. Samples (10 µl) were injected onto an Ascentis C18 column (particle size of 2.7 µm, 50 × 2.10 mm, Supelco). The mobile phase flow rate was 0.3 ml min$^{-1}$. Mobile phase A was 100% (vol/vol) Milli-Q water with 0.1% formic acid, and mobile phase B (MPB) was 100% (vol/vol) methanol with 0.1% formic acid. The mobile phase-gradient sequence (vol/vol) was initiated with 50% MPB, linearly increased to 90% MPB over 1.2 min and was held for 0.5 min and then returned to 50% MPB over 0.8 min and was held for 1.5 min leading. Ion transitions for celecoxib and the internal standard were 382.10–361.90 *m*/*z* and 336.2–195.0 *m*/*z*. Celecoxib and the internal standard eluted at 1.8 min and 1.6 min. The assay was validated by assay of $n = 3$–5 quality-control samples and found to be accurate and precise (<10% variation).

**Statistical analysis.** Statistics were analysed using GraphPad Prism version 8 and version 9 (GraphPad Software). Data are presented as mean ± s.e.m. For statistical analysis of smaller groups ($n < 5$), we employed a Mann–Whitney test. For larger groups ($n > 5$), a Student's *t*-test or one-way or two-way ANOVA followed by Dunnett's or Tukey's multiple-comparisons test was used for statistical comparisons. When employing parametric tests (*t*-test or ANOVA), normal distribution of data was confirmed using a Shapiro–Wilk test or the D'Agostino–Pearson test. *A P* value less than 0.05 was considered statistically significant.

**Reporting Summary.** Further information on research design is available in the Nature Research Reporting Summary linked to this article.

## Data availability

All data generated or analysed during this study are included in this published article (and its Supplementary Information). Data that support the findings of this study are available from the corresponding authors upon request. The exception is lipidomic data, which will be available in the NIH Metabolomics Workbench repository at https://doi.org/10.21228/M8GH59. Source data are provided with this paper.

Received: 25 February 2020; Accepted: 13 August 2021;
Published online: 20 September 2021

## References

1. Alitalo, K. The lymphatic vasculature in disease. *Nat. Med.* **17**, 1371–1380 (2011).
2. Bernier-Latmani, J. & Petrova, T. V. Intestinal lymphatic vasculature: structure, mechanisms and functions. *Nat. Rev. Gastroenterol. Hepatol.* **14**, 510–526 (2017).

3. Trevaskis, N. L., Kaminskas, L. M. & Porter, C. J. From sewer to saviour—targeting the lymphatic system to promote drug exposure and activity. *Nat. Rev. Drug Discov.* **14**, 781–803 (2015).
4. Petrova, T. V. & Koh, G. Y. Organ-specific lymphatic vasculature: from development to pathophysiology. *J. Exp. Med.* **215**, 35–49 (2018).
5. Stacker, S. A. et al. Lymphangiogenesis and lymphatic vessel remodelling in cancer. *Nat. Rev. Cancer* **14**, 159–172 (2014).
6. Swartz, M. A. Immunomodulatory roles of lymphatic vessels in cancer progression. *Cancer Immunol. Res.* **2**, 701–707 (2014).
7. Schwager, S. & Detmar, M. Inflammation and lymphatic function. *Front. Immunol.* **10**, 1016–1028 (2019).
8. Maisel, K., Sasso, M. S., Potin, L. & Swartz, M. A. Exploiting lymphatic vessels for immunomodulation: rationale, opportunities, and challenges. *Adv. Drug Deliv. Rev.* **114**, 43–59 (2017).
9. Louveau, A. et al. CNS lymphatic drainage and neuroinflammation are regulated by meningeal lymphatic vasculature. *Nat. Neurosci.* **21**, 1380–1391 (2018).
10. Louveau, A. et al. Structural and functional features of central nervous system lymphatic vessels. *Nature* **523**, 337–341 (2015).
11. Da Mesquita, S. et al. Functional aspects of meningeal lymphatics in ageing and Alzheimer's disease. *Nature* **560**, 185–191 (2018).
12. Aspelund, A. et al. A dural lymphatic vascular system that drains brain interstitial fluid and macromolecules. *J. Exp. Med.* **212**, 991–999 (2015).
13. Ma, Q., Ineichen, B. V., Detmar, M. & Proulx, S. T. Outflow of cerebrospinal fluid is predominantly through lymphatic vessels and is reduced in aged mice. *Nat. Commun.* **8**, 1434 (2017).
14. Zhang, F. et al. Lacteal junction zippering protects against diet-induced obesity. *Science* **361**, 599–603 (2018).
15. Blum, K. S. et al. Chronic high-fat diet impairs collecting lymphatic vessel function in mice. *PLoS ONE* **9**, e94713 (2014).
16. Hespe, G. E. et al. Exercise training improves obesity-related lymphatic dysfunction. *J. Physiol.* **594**, 4267–4282 (2016).
17. Torrisi, J. S. et al. Inhibition of Inflammation and iNOS improves lymphatic function in obesity. *Sci. Rep.* **6**, 19817 (2016).
18. Weitman, E. S. et al. Obesity impairs lymphatic fluid transport and dendritic cell migration to lymph nodes. *PLoS ONE* **8**, e70703 (2013).
19. Arngrim, N., Simonsen, L., Holst, J. J. & Bülow, J. Reduced adipose tissue lymphatic drainage of macromolecules in obese subjects: a possible link between obesity and local tissue inflammation? *Int. J. Obes.* **37**, 748–750 (2012).
20. Greene, A. K., Grant, F. D. & Slavin, S. A. Lower-extremity lymphedema and elevated body-mass index. *N. Engl. J. Med.* **366**, 2136–2137 (2012).
21. Klimontov, V. et al. The relationships between serum levels of adipokines, body fat distribution, and subcutaneous microvasculature in type 2 diabetic subjects. *Diabetes* **67**, 2055-P (2018).
22. Boyages, J. et al. Liposuction for advanced lymphedema: a multidisciplinary approach for complete reduction of arm and leg swelling. *Ann. Surg. Oncol.* **22**, S1263–S1270 (2015).
23. Dagenais, S. L. et al. Foxc2 is expressed in developing lymphatic vessels and other tissues associated with lymphedema-distichiasis syndrome. *Gene Expr. Patterns* **4**, 611–619 (2004).
24. Sawane, M. et al. Apelin inhibits diet-induced obesity by enhancing lymphatic and blood vessel integrity. *Diabetes* **62**, 1970–1980 (2013).
25. Harvey, N. L. et al. Lymphatic vascular defects promoted by *Prox1* haploinsufficiency cause adult-onset obesity. *Nat. Genet.* **37**, 1072–1081 (2005).
26. Dellinger, M. T., Hunter, R. J., Bernas, M. J., Witte, M. H. & Erickson, R. P. Chy-3 mice are *Vegfc* haploinsufficient and exhibit defective dermal superficial to deep lymphatic transition and dermal lymphatic hypoplasia. *Dev. Dyn.* **236**, 2346–2355 (2007).
27. Lee, Y. et al. Enhanced lymphangiogenesis and lymphatic function protects diet-induced obesity and insulin resistance. *FASEB J.* **33**, 662.25 (2019).
28. Lee, M.-J., Wu, Y. & Fried, S. K. Adipose tissue heterogeneity: implication of depot differences in adipose tissue for obesity complications. *Mol. Aspects Med.* **34**, 1–11 (2013).
29. Liu, J. et al. Impact of abdominal visceral and subcutaneous adipose tissue on cardiometabolic risk factors: the Jackson Heart Study. *J. Clin. Endocrinol. Metab.* **95**, 5419–5426 (2010).
30. Raajendiran, A., Tsiloulis, T. & Watt, M. J. Adipose tissue development and the molecular regulation of lipid metabolism. *Essays Biochem.* **60**, 437–450 (2016).
31. Ji, Y., Sakata, Y. & Tso, P. Nutrient-induced inflammation in the intestine. *Curr. Opin. Clin. Nutr. Metab. Care* **14**, 315–321 (2011).
32. Scallan, J. P., Hill, M. A. & Davis, M. J. Lymphatic vascular integrity is disrupted in type 2 diabetes due to impaired nitric oxide signaling. *Cardiovasc. Res.* **107**, 89–97 (2015).
33. Zawieja, S. D. et al. Impairments in the intrinsic contractility of mesenteric collecting lymphatics in a rat model of metabolic syndrome. *Am. J. Physiol. Heart Circ. Physiol.* **302**, H643–H653 (2012).
34. Kuan, E. L. et al. Collecting lymphatic vessel permeability facilitates adipose tissue inflammation and distribution of antigen to lymph node-homing adipose tissue dendritic cells. *J. Immunol.* **194**, 5200–5210 (2015).
35. Koenig, A. & Thaunat, O. Lymphoid neogenesis and tertiary lymphoid organs in transplanted organs. *Front. Immunol.* **7**, 646 (2016).
36. Ruddle, N. H. Lymphatic vessels and tertiary lymphoid organs. *J. Clin. Invest.* **124**, 953–959 (2014).
37. Escobedo, N. et al. Restoration of lymphatic function rescues obesity in *Prox1*-haploinsufficient mice. *JCI Insight* **1**, e85096 (2016).
38. Donath, M. Y. Targeting inflammation in the treatment of type 2 diabetes: time to start. *Nat. Rev. Drug Discov.* **13**, 465–476 (2014).
39. Kahn, S. E., Cooper, M. E. & Del Prato, S. Pathophysiology and treatment of type 2 diabetes: perspectives on the past, present, and future. *Lancet* **383**, 1068–1083 (2014).
40. Su, J.-L. et al. Cyclooxygenase-2 induces EP1- and HER-2/Neu-dependent vascular endothelial growth factor-C up-regulation: a novel mechanism of lymphangiogenesis in lung adenocarcinoma. *Cancer Res.* **64**, 554–564 (2004).
41. Hosono, K. et al. Roles of prostaglandin E2–EP3/EP4 receptor signaling in the enhancement of lymphangiogenesis during fibroblast growth factor-2-induced granulation formation. *Arterioscler. Thromb. Vasc. Biol.* **31**, 1049–1058 (2011).
42. El-Bahrawy, H., Hegazy, S., Farrag, W. & Werida, R. Targeting inflammation using celecoxib with glimepiride in the treatment of obese type 2 diabetic Egyptian patients. *Int. J. Diabetes Dev. Ctries* **37**, 97–102 (2017).
43. Hsieh, P.-S. et al. COX-2-mediated inflammation in fat is crucial for obesity-linked insulin resistance and fatty liver. *Obesity* **17**, 1150–1157 (2009).
44. Karaman, S. et al. Blockade of VEGF-C and VEGF-D modulates adipose tissue inflammation and improves metabolic parameters under high-fat diet. *Mol. Metab.* **4**, 93–105 (2014).
45. Karaman, S. et al. Transgenic overexpression of VEGF-C induces weight gain and insulin resistance in mice. *Sci. Rep.* **6**, 31566 (2016).
46. Han, S. et al. Targeted delivery of a model immunomodulator to the lymphatic system: comparison of alkyl ester versus triglyceride mimetic lipid prodrug strategies. *J. Control. Release* **177**, 1–10 (2014).
47. Hu, L. et al. Glyceride-mimetic prodrugs incorporating self-immolative spacers promote lymphatic transport, avoid first-pass metabolism, and enhance oral bioavailability. *Angew. Chem. Int. Ed.* **55**, 13700–13705 (2016).
48. Adams, J. M. et al. Ceramide content is increased in skeletal muscle from obese insulin-resistant humans. *Diabetes* **53**, 25–31 (2004).
49. Turpin, S. M. et al. Obesity-induced CerS6-dependent C16:0 ceramide production promotes weight gain and glucose intolerance. *Cell Metab.* **20**, 678–686 (2014).
50. Holland, W. L. et al. Inhibition of ceramide synthesis ameliorates glucocorticoid-, saturated-fat-, and obesity-induced insulin resistance. *Cell Metab.* **5**, 167–179 (2007).
51. Boon, J. et al. Ceramides contained in LDL are elevated in type 2 diabetes and promote inflammation and skeletal muscle insulin resistance. *Diabetes* **62**, 401–410 (2013).
52. Anzai, K. et al. Increased lipid absorption and transport in the small intestine of Zucker obese rats. *J. Clin. Biochem. Nutr.* **45**, 82–85 (2009).
53. Lu, W. J. et al. The regulation of the lymphatic secretion of glucagon-like peptide-1 (GLP-1) by intestinal absorption of fat and carbohydrate. *Am. J. Physiol. Gastrointest. Liver Physiol.* **293**, G963–G971 (2007).
54. Miura, S. et al. Increased proliferative response of lymphocytes from intestinal lymph during long chain fatty acid absorption. *Immunology* **78**, 142–146 (1993).
55. Harvey, N. L. The link between lymphatic function and adipose biology. *Ann. NY Acad. Sci.* **1131**, 82–88 (2008).
56. Raajendiran, A. et al. Proteome analysis of human adipocytes identifies depot-specific heterogeneity at metabolic control points. *Am. J. Physiol.-Endocrinol. Metab.* **1**, E1068–E1084 (2021).
57. Escobedo, N. & Oliver, G. The lymphatic vasculature: its role in adipose metabolism and obesity. *Cell Metab.* **26**, 598–609 (2017).
58. Trevaskis, N. L. et al. Intestinal lymph flow, and lipid and drug transport scale allometrically from pre-clinical species to humans. *Front. Physiol.* **11**, 458 (2020).
59. Chi, J. et al. Three-dimensional adipose tissue imaging reveals regional variation in beige fat biogenesis and PRDM16-dependent sympathetic neurite density. *Cell Metab.* **27**, 226–236 (2018).
60. Schindelin, J. et al. Fiji: an open-source platform for biological-image analysis. *Nat. Methods* **9**, 676–682 (2012).
61. Trevaskis, N. L. et al. The mesenteric lymph duct cannulated rat model: application to the assessment of intestinal lymphatic drug transport. *J. Vis. Exp.* https://doi.org/10.3791/52389 (2015).
62. Trevaskis, N. L. et al. A mouse model to evaluate the impact of species, sex, and lipid load on lymphatic drug transport. *Pharm. Res.* **30**, 3254–3270 (2013).
63. Tsiloulis, T. et al. Impact of endurance exercise training on adipocyte microRNA expression in overweight men. *FASEB J.* **31**, 161–171 (2017).

64. Livak, K. J. & Schmittgen, T. D. Analysis of relative gene expression data using real-time quantitative PCR and the $2^{-\Delta\Delta C(T)}$ method. *Methods* **25**, 402–408 (2001).
65. Roy, D., Perreault, M. & Marette, A. Insulin stimulation of glucose uptake in skeletal muscles and adipose tissues in vivo is NO dependent. *Am. J. Physiol.* **274**, E692–E699 (1998).
66. Stone, K. P., Wanders, D., Orgeron, M., Cortez, C. C. & Gettys, T. W. Mechanisms of increased in vivo insulin sensitivity by dietary methionine restriction in mice. *Diabetes* **63**, 3721–3733 (2014).
67. Krebs buffer (10×, pH 7.2). *Cold Spring Harb. Protoc.* https://doi.org/10.1101/pdb.rec11255 (2007).
68. Weigmann, B. et al. Isolation and subsequent analysis of murine lamina propria mononuclear cells from colonic tissue. *Nat. Protoc.* **2**, 2307–2311 (2007).
69. Nishimura, S. et al. $CD8^+$ effector T cells contribute to macrophage recruitment and adipose tissue inflammation in obesity. *Nat. Med.* **15**, 914–920 (2009).
70. Aurelio, L. et al. From sphingosine kinase to dihydroceramide desaturase: a structure–activity relationship (SAR) study of the enzyme inhibitory and anticancer activity of 4-((4-(4-chlorophenyl)thiazol-2-yl)amino)phenol (SKI-II). *J. Med. Chem.* **59**, 965–984 (2016).
71. Creek, D. J., Jankevics, A., Burgess, K. E., Breitling, R. & Barrett, M. P. IDEOM: an Excel interface for analysis of LC–MS-based metabolomics data. *Bioinformatics* **28**, 1048–1049 (2012).
72. Sumner, L. W. et al. Proposed minimum reporting standards for chemical analysis Chemical Analysis Working Group (CAWG) Metabolomics Standards Initiative (MSI). *Metabolomics* **3**, 211–221 (2007).
73. Chong, J. et al. MetaboAnalyst 4.0: towards more transparent and integrative metabolomics analysis. *Nucleic Acids Res.* **46**, W486–W494 (2018).
74. Andrikopoulos, S., Blair, A. R., Deluca, N., Fam, B. C. & Proietto, J. Evaluating the glucose tolerance test in mice. *Am. J. Physiol. Endocrinol. Metab.* **295**, E1323–E1332 (2008).
75. Lancaster, G. I. & Henstridge, D. C. Body composition and metabolic caging analysis in high fat fed mice. *J. Vis. Exp.* https://doi.org/10.3791/57280 (2018).

## Acknowledgements

We thank the Monash Animal Research Platform; the Imaging and FACS core at the Monash Institute of Pharmaceutical Sciences, particularly S. Fung for technical support; the Melbourne Mouse Metabolic Phenotyping Platform, particularly V. Haynes for technical support; T. Karnezis, St. Vincent's Institute, Melbourne, for providing human adipocytes and T. Tsiloulis, J.C.Y. Lo, D. Senyschyn and G. Chen for technical assistance. We sincerely thank surgeons G. Beban, N. Evenett, P. Johnston and A. Bartlett for their assistance with human mesenteric adipose tissue collection. This work was supported by project grants from the National Health and Medical Research Council of Australia (NHMRC grant 1100036 and NHMRC grant 1177084) and the Health Research Council of New Zealand (HRC 16-036) and the Hugo Charitable Trust (New Zealand).

## Author contributions

E.C. conducted the majority of the experimental work, wrote the main paper and designed and interpreted experiments; N.L.T. was the main supervisor of E.C., conducted some adipocyte studies, wrote the main paper and designed and interpreted the work; C.J.H.P. and M.J.W. substantially revised the paper, co-supervised E.C. and contributed to experimental design and interpretation; M.J.W. also assisted with some metabolic analyses; C.J.N. optimized imaging methods and analysis and revised sections of the manuscript and methods related to imaging analysis; T.Q. synthesized and helped design the celecoxib prodrug and wrote methods for prodrug synthesis; J.S.S. facilitated the design and synthesis of the celecoxib prodrug and revised methods for prodrug synthesis; L.H. co-supervised E.C. and contributed to experimental design and interpretation; S.A., G.G., V.D.M.F., H.C. and A.L. conducted analyses such as ELISA, flow cytometry and metabolic analyses; G.S. conducted light-sheet microscopy analysis of human adipose tissue samples; J.A.W., A.R.J.P., J.H., A.B.J.E. and K.L.P. collected human samples, assisted with data interpretation and revised the manuscript; N.L.H. assisted with design and interpretation of lymphatic analyses and revised the manuscript. A.S., D.J.C. and D.A. conducted the metabolomic analysis, assisted with interpretation and presentation of metabolomic data and revised sections of the manuscript and methods related to the metabolomic analysis.

## Competing interests

C.J.H.P., N.L.T., T.Q., J.S.S., E.C. and M.J.W. are inventors of the lymph-directing glyceride prodrug technology described in the text (PCT/AU2020/050997). This technology has been patented and licensed via a commercial agreement with PureTech Health. PureTech Health has subsequently entered into a collaboration agreement with Boehringer Ingelheim to explore the technology in immune modulation. J.S.S. and T.Q. are currently employed by PureTech Health. The remaining authors declare no competing interests.

## Additional information

**Extended data** is available for this paper at https://doi.org/10.1038/s42255-021-00457-w.

**Supplementary information** The online version contains supplementary material available at https://doi.org/10.1038/s42255-021-00457-w.

**Correspondence and requests for materials** should be addressed to Enyuan Cao, Christopher J. H. Porter or Natalie L. Trevaskis.

**Peer review information** *Nature Metabolism* thanks Stephan Herzig, Joseph Rutkowski and the other, anonymous, reviewers for their contribution to the peer review of this work. Primary Handling Editor: Christoph Schmitt

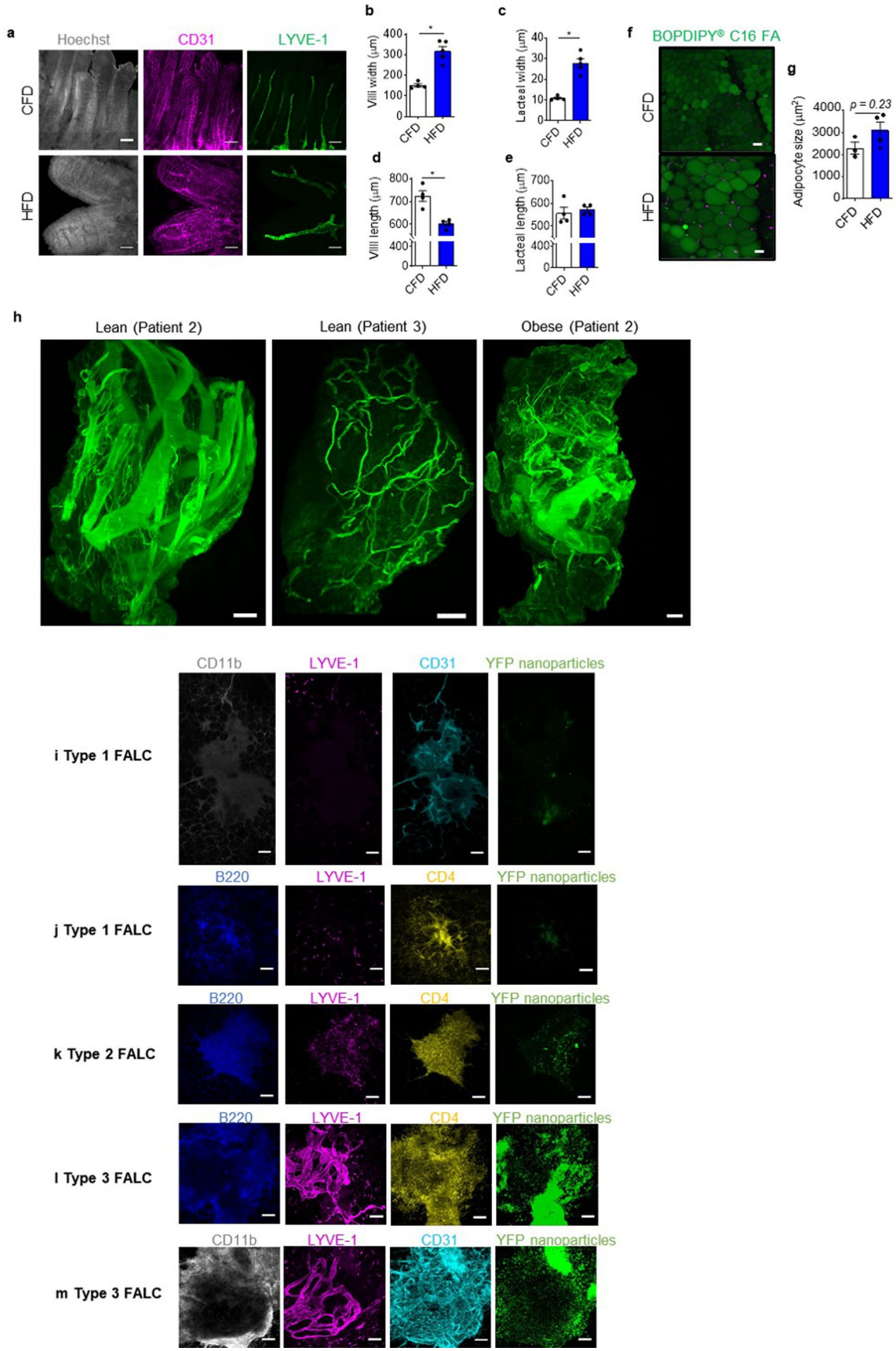


**Extended Data Fig. 1 | See next page for caption.**

**Extended Data Fig. 1 | HFD-associated changes to intestinal villi and lacteals, and adipocytes and FALC in VAT. a**, Representative immunofluorescence images of intestinal villi. Cell nuclei (Hoechst, grey), CD31 + blood vessels (pink) and LYVE-1+ lacteals (green). Scale bars, 100 μm. **b-e**, Quantification of the width and length of the intestinal villi and lacteals from immunofluorescence images. **f**, Representative immunofluorescence images of VAT tissue stained for lipid droplets (green, Bodipy C16 FA). Scale bar, 50 μm. **g**, Quantification of adipocyte size (μm2). Mean ± s.e.m, n = 4, 5 mice in (**b-c**), n = 4, 4 mice in (**d-e**) with 3-4 intestinal villi analysed per mouse, n = 3, 3 mice in **(g)**. Statistical differences, *$p < 0.05$ from two-tailed Mann-Whitney test. **h**, Immunofluorescent images of podoplanin + (green) lymphatic vessels in mesenteric adipose tissue from lean patient 2 and 3 and obese patient 2. Images from lean patient 1 and obese patient 2 are in Fig. 1c. (**i-m**) Representative immunofluorescence images of lymphatic vessels (LYVE-1 +, pink), blood vessels (CD31 +, cyan), CD11b + myeloid cells (grey), CD4 + T cells (yellow), B220 + B cells (blue), and YFP particles (green) in FALCs from mice fed CFD or HFD for 32 weeks. **i-j**, Type 1 FALCs were rich in CD31 + blood vessels, T cells and B cells but lacked CD11b + and LYVE + cells (that is LECs and macrophages) and had relatively low uptake of YFP-nanoparticles. **k**, Type 2 FALCs were rich in T cells, B cells and LYVE-1+ cells (macrophages or LEC) but had no observable lymphatic vessels and moderate uptake of YFP-nanoparticles. **l-m**, Type 3 FALCs contained, and were in close proximity to, LYVE-1+ lymphatic vessels and CD31 + blood vessels. The lymphatic vessels appeared disorganised and lacked a clear orientation toward a collecting lymphatic vessel. Type 3 FALCs also contained high numbers of T cells, B cells and myeloid cells. The observed overlap in staining between the YFP nanoparticles and CD11b + myeloid cells is most likely due to phagocytosis of the particles by the cells. Scale bars, 100 μm (**i-m**). (**i-m**) Representative of images from 2-3 FALCs for n = 5 mice. P values and details of the statistical testing are provided as source data.

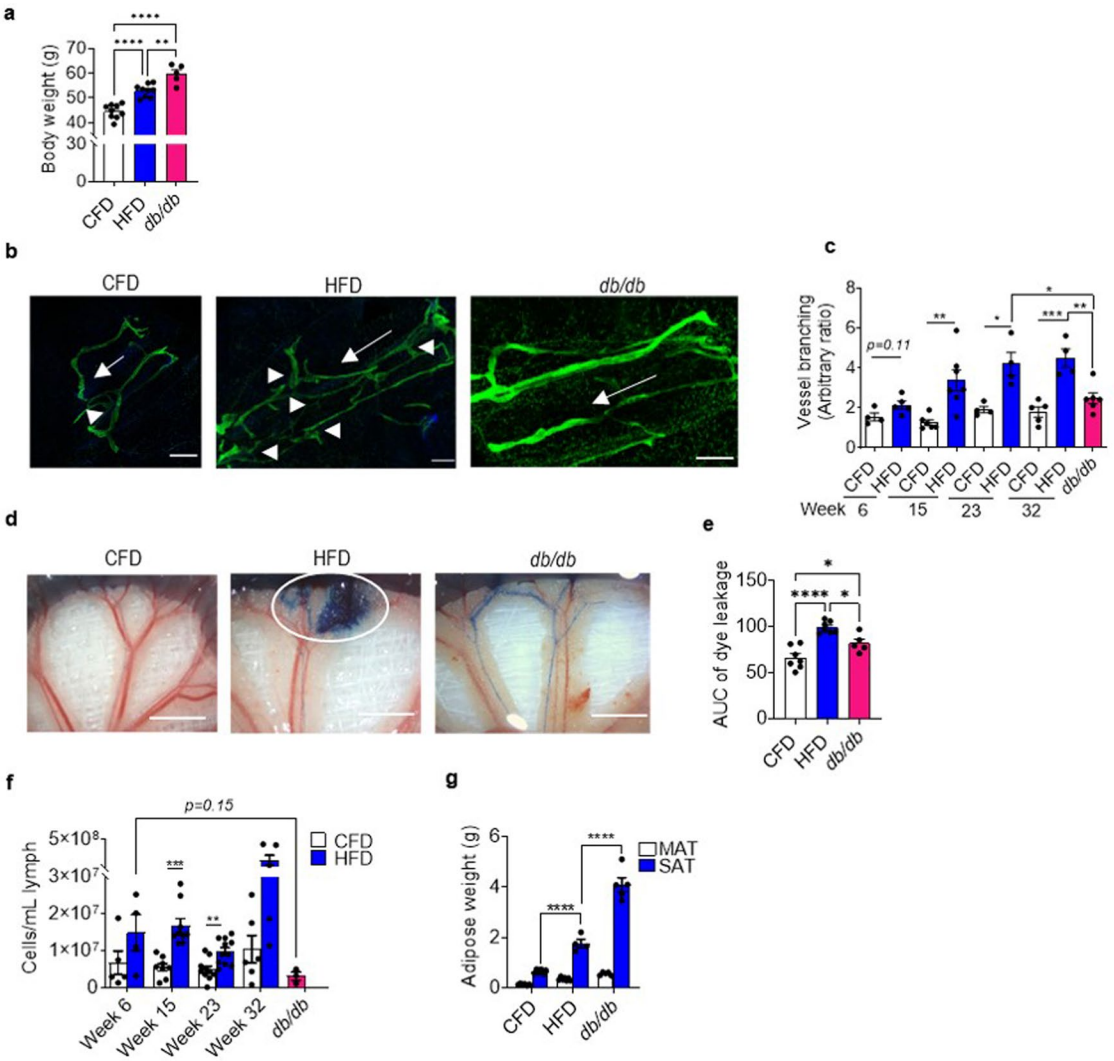


**Extended Data Fig. 2 | An examination of mesenteric lymphatic dysfunction in 15-17 week old CFD fed db/db mice in comparison to C57BL/6 mice fed a CFD or HFD for 6, 15, 23 or 32 weeks from 6-7 weeks of age. a**, Total body weight. Mean ± s.e.m for n = 9, 9, 5. **b**, Representative immunofluorescence images of the mesenteric lymphatic vessels (LYVE-1 (green)) in VAT of db/db and C57BL/6 mice. Note white arrow indicates the direction of lymph flow, arrow heads indicate point of vessel branching. Scale bar, 500 μm. **c**, Quantification of mesenteric lymphatic vessel branching in VAT of mice. Mean ± s.e.m for n = 4 or n = 5 mice for week 6, n = 6 or n = 7 mice for week 15, n = 4 or n = 5 mice for week 23, n = 4 or n = 5 mice for week 32 and n = 5 for db/db mice. **d**, Representative images of Evans blue dye passage through mesenteric lymphatic vessels and leakage to VAT 10 min after intramucosal dye injection to CFD and HFD fed C57BL/6 mice and db/db mice. Scale bar, 5 mm. White circle highlights a site of lymph leakage. **e**, Area under the curve (AUC) of the Evan's blue dye intensity plots. Mean ± s.e.m., n = 7, 7 and 5 mice. **f**, Total cells in mesenteric lymph of mice fed CFD or HFD for 6, 15, 23, 32 weeks or db/db mice fed CFD. Mean ± s.e.m for n = 5 or n = 4 mice for week 6, n = 8 or n = 9 mice for week 15, n = 6 or n = 6 mice for week 32 and n = 3 for db/db mice. **g**, Weight of subcutaneous adipose tissue (SAT, inguinal adipose tissue depot) and mesenteric adipose tissue (MAT). Note comparisons across CFD, HFD and db/db mice in (**b, d, e, g**) are made between C57BL/6 mice fed CFD or HFD for 23 weeks and db/db mice age 15-17 weeks. Statistical differences, *$p < 0.05$, **$p < 0.01$, ***$p < 0.005$, or ****$p < 0.0001$ from (**a, e**) one-way ANOVA, **(c)** two-tailed Mann-Whitney test for week 6, 23 and 32 data, two-tailed Student's t test was used for week 15 data, one-way ANOVA was used for comparison between db/db mice and week 23 and week 32 data, **(f)** a two-tailed Student's t-test (except one-way ANOVA was used for comparison between db/db mice vs week 6 data), **(g)** two-way ANOVA. P values and details of the statistical testing are provided as source data.

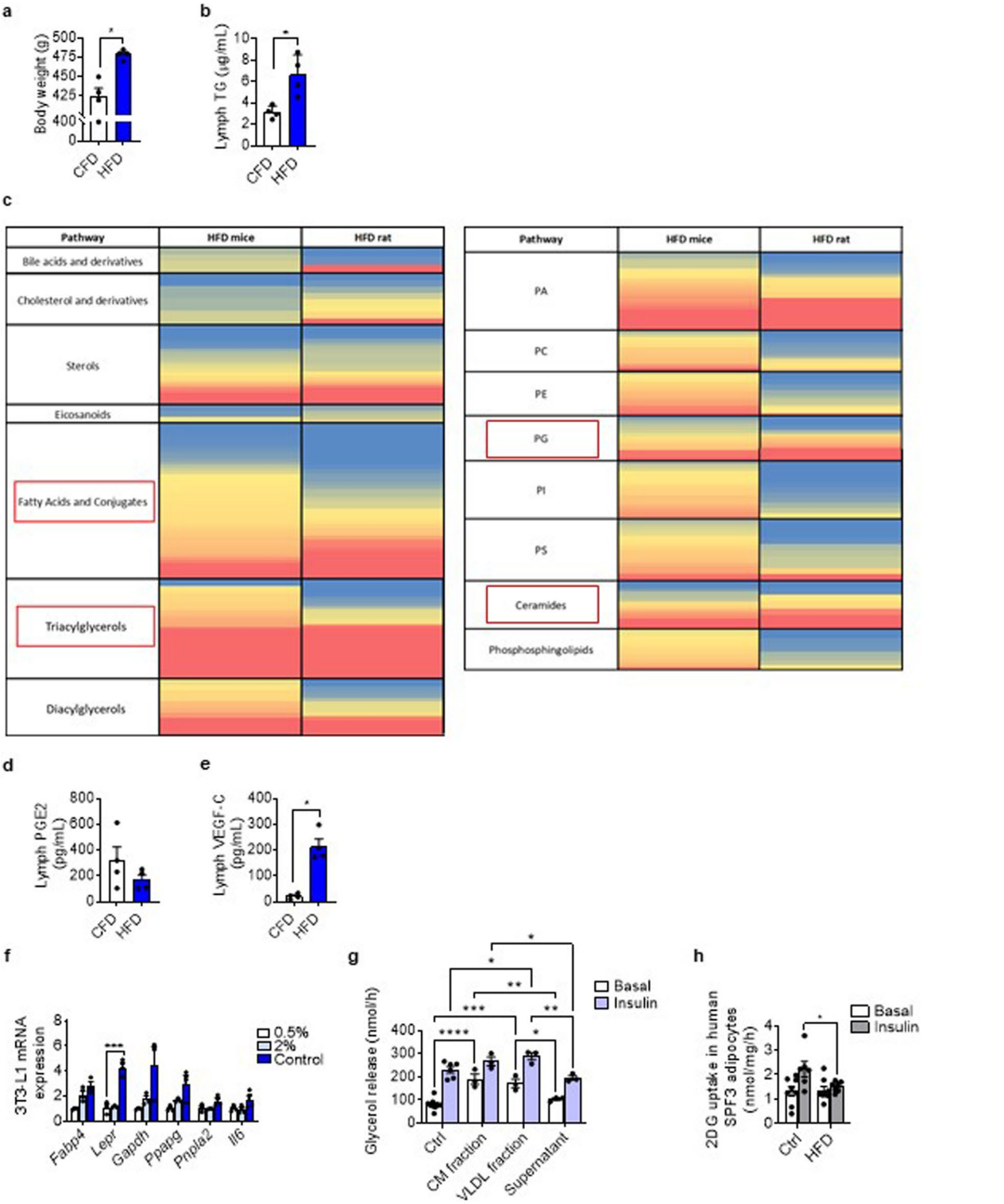


**Extended Data Fig. 3 | Body weight, and composition and effects of mesenteric lymph from Sprague-Dawley rats fed CFD or HFD for 6-9 weeks. a**, Body weight and **b**, TG concentration. Mean ± s.e.m for n = 4, 4 (HFD) rats. **c**, Heatmap analysis of lipidomics data of lymph from HFD mice and rats, expressed as mean peak intensity relative to CFD mice and rats, respectively. Blue indicates decreased abundance, red indicates increase and yellow signifies no change. n = 4, 4 mice/rats. **d-e**, PGE2 and VEGFc concentration in mesenteric lymph of rats. Mean ± s.e.m, n = 4, 4 rats. Statistical differences, *p < 0.05 from two-tailed Mann-Whitney test. **f**, Real time PCR analysis of Fabp4, Lepr, Gapdh, Pparg, Pnpla2, and Il6 mRNA expression in 3T3-L1 adipocytes treated with control media (Ctrl) or 0.5 or 2% v/v CFD-lymph in media. Mean ± s.e.m. for n = 3 from N = 1 experiment. **g**, Lipolysis in mature 3T3-L1 adipocytes (from glycerol release) in basal and forskolin-stimulated conditions after treatment with control media (Ctrl) or 2% lymph chylomicron (CM), VLDL or lipid-free protein fraction (supernatant). Mean ± s.e.m. for n = 3 except Ctrl (n = 9 (basal) and n = 6 (forskolin)) from N = 1 experiment. Statistical differences, *p < 0.05, **p < 0.01, ***p < 0.005, ****p < 0.001 from Two-Way ANOVA. **h**, 14C-2-deoxyglucose (2DG) uptake into SPF3 human adipocytes in basal and insulin-stimulated conditions after treatment with control media or 2% HFD rat lymph. Mean ± s.e.m. for n = 8, 8 (basal) and n = 6, 7 (insulin) replicates from N = 3 experiments. Statistical differences, *p < 0.05 from two-way ANOVA. P values and details of the statistical testing are provided as source data.

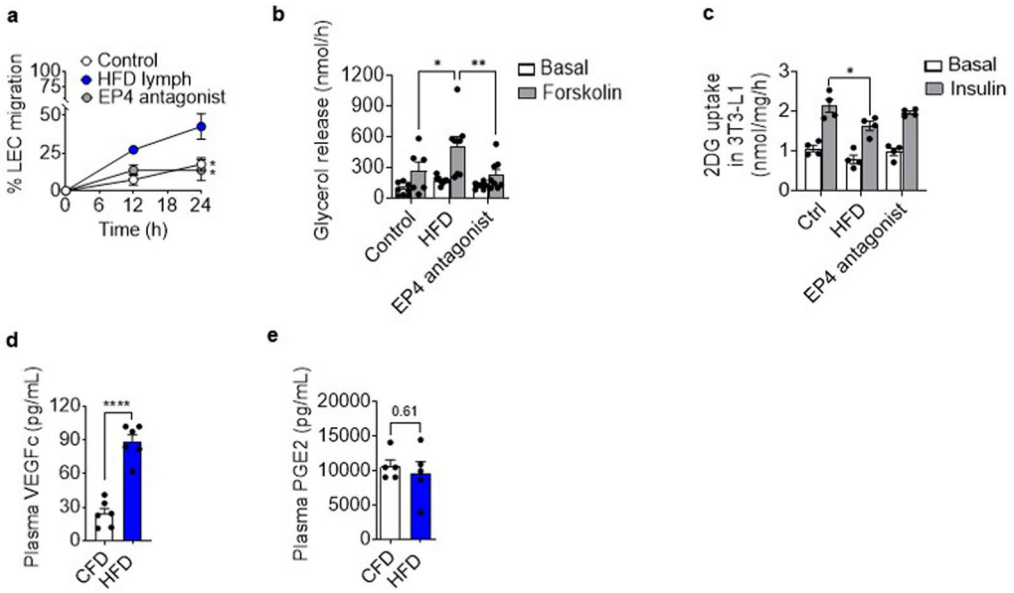


**Extended Data Fig. 4 | The impact of EP4 inhibition on HFD-lymph induced LEC migration, adipocyte lipolysis and adipocyte insulin sensitivity. a**, LEC migration over time on incubation with control media or 2% v/v HFD-lymph from mice ± EP4 antagonist, L-161,982. Mean ± s.e.m for n = 9, 7, 10 from N = 2 experiments. **b**, Lipolysis in mature 3T3-L1 adipocytes (from glycerol release) in basal and forskolin-stimulated conditions on incubation with control media or 2% v/v HFD-lymph from mice ± EP4 antagonist. Mean ± s.e.m for n = 8, 8, 8 (basal) and 6, 9, 8 (forskolin) replicates from N = 2 experiments. **c**, 14C-2-deoxyglucose (2DG) uptake into mature 3T3-L1 adipocytes in basal and insulin-stimulated conditions on incubation with control media or 2% v/v HFD-lymph from mice ± EP4 antagonist. Mean ± s.e.m. for n = 4 (basal) and n = 4 (insulin) replicates of N = 2 experiments. Statistical differences **(a)** *$p < 0.05$ from one-way ANOVA and (**b-c**) *$p < 0.05$, **$p < 0.01$ from two-way ANOVA. **d-e**, PGE2 and VEGFc concentration in plasma of mice fed CFD or HFD for 22-23 weeks. Mean ± s.e.m., n = 6, 6 (plasma VEGFc) and n = 5, 5 (plasma PGE2) mice. Statistical differences, ****$p < 0.001$ from two-tailed Student's t-test. P values and details of the statistical testing are provided as source data.

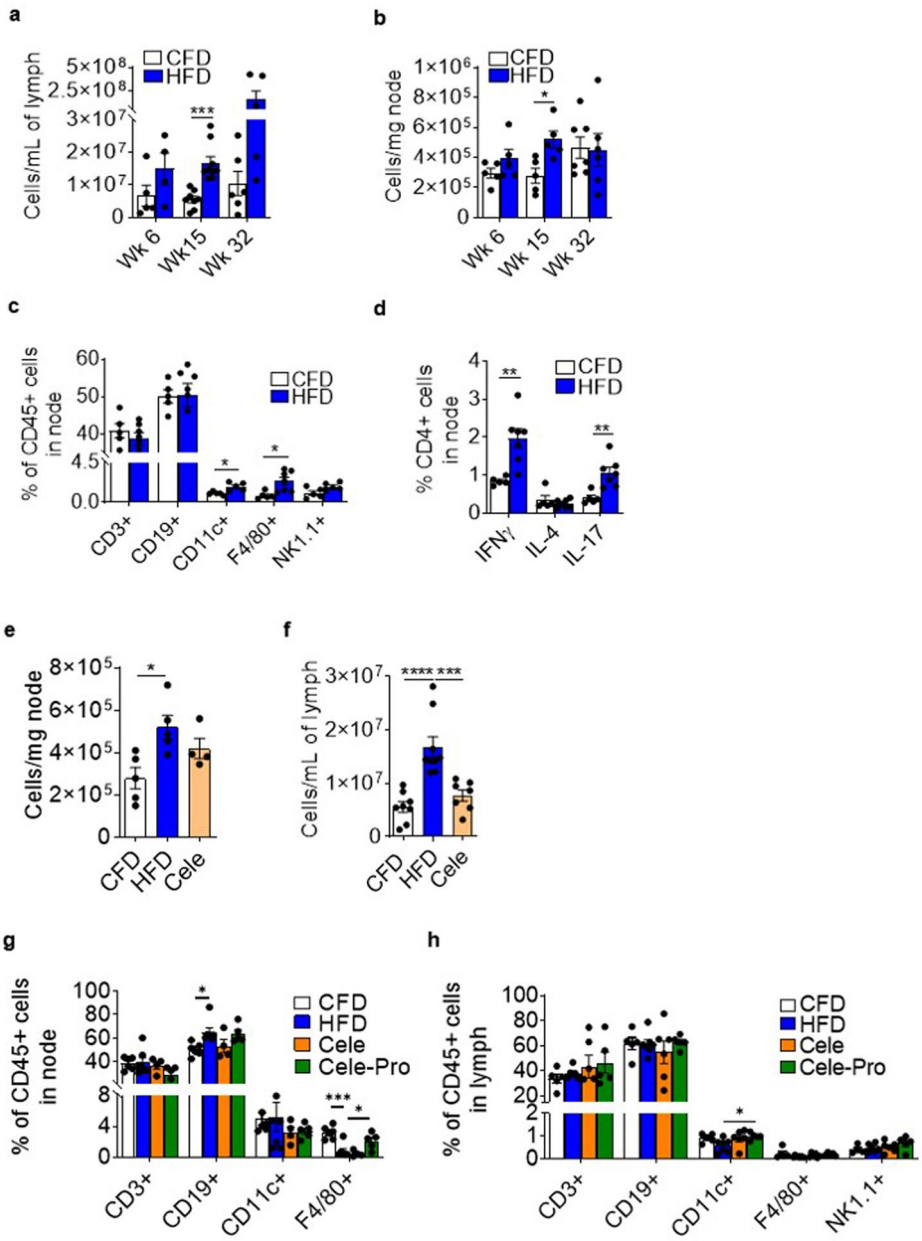


**Extended Data Fig. 5 | Immune cell accumulation in mesenteric lymph fluid and lymph nodes across prevention and treatment groups. a-b**, Total immune cells in mesenteric lymph fluid and lymph nodes. Mean ± s.e.m., **(a)** n = 5, 4 (week 6), n = 8, 9 (week 15), n = 6, 6 (week 32). **(b)** n = 5, 5 (week 6), n = 5, 5 (week 15), n = 6, 6 (week 32). **c**, Percent of CD45 + cells that were T cells (CD3 + ), B cells (CD19 + ), dendritic cells (CD11c + ), macrophages (F4/80 + ) and NK cells (NK1.1), and **d**, Percent of T cells that were Th1 (IFNγ + ), Th2 (IL-4 + ) and Th17 (IL-17 + ) cells in mesenteric lymph nodes of mice fed CFD or HFD for 6, 15 or 32 weeks. (c-d) all data at week 15 with n = 5 (CFD), 7 (HFD, except n = 5 for CD11c + and NK1.1+ cells). **e**, **f**, Total immune cells in mesenteric lymph fluid or node of mice fed with CFD, HFD or HFD plus Celecoxib (Cele) for 15 weeks (prevention study, see timeline Fig. 4e). Mean ± s.e.m., **(e)** n = 5, 5, 4. **(f)** n = 9, 10, 7. **g-h**, Percent of CD45 + cells that were T cells (CD3 + ), B cells (CD19 + ), dendritic cells (CD11c + ), macrophages (F4/80 + ) and NK cells (NK1.1) in mesenteric lymph fluid or nodes of mice fed with CFD, HFD or HFD plus celecoxib or Cele-Pro (treatment study, see timeline Fig. 5a). Mean ± s.e.m., **(g)** n = 6, 7, 4, 5 and **(h)** n = 5, 7, 6, 5 (except n = 4 for CFD NK1.1+ cells, n = 6 for HFD CD3 + cells and n = 6 HFD NK1.1+ cells). Statistical differences from two-tailed Student's t-test (**a-d**) or one-way ANOVA (**e-h**), *p < 0.05, **p < 0.01, ***p < 0.005, ****p < 0.001. P values and details of the statistical testing are provided as source data.

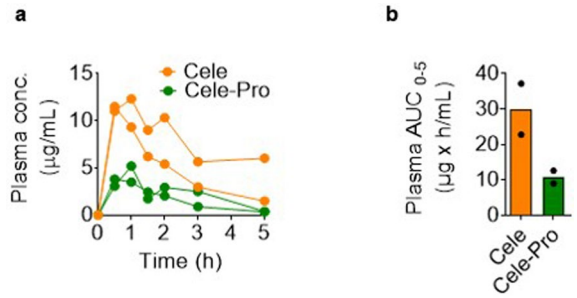


**Extended Data Fig. 6 | Systemic exposure of celecoxib in mice administered celecoxib (Cele) or celecoxib prodrug (Cele-Pro). a**, Plasma concentrations of celecoxib over time in individual mice, and **b**, Area under the curve (AUC) of celecoxib plasma concentration versus time profile from time 0-5 h following oral gavage of 29 mg/kg Cele or 29 mg/kg Cele-Pro to fasted mice in a lipid based formulation. Mean of n = 2.

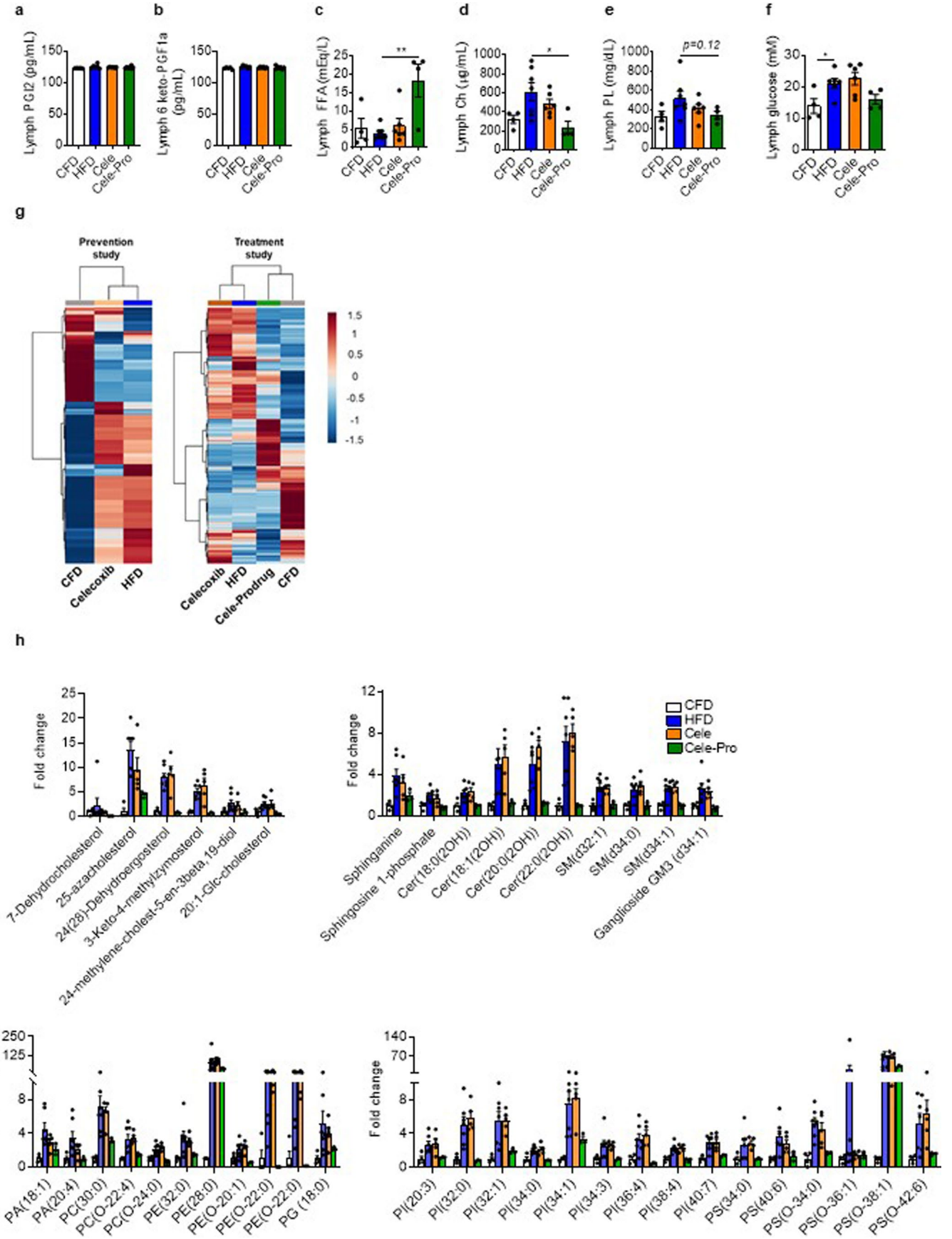


**Extended Data Fig. 7 | See next page for caption.**

**Extended Data Fig. 7 | Lipid metabolites in mesenteric lymph fluid obtained from mice fed a CFD, HFD, HFD plus celecoxib or celecoxib prodrug (Cele-Pro). a**-**b**, PGI2 and 6 keto-PGF1a concentrations in mesenteric lymph from CFD, HFD, HFD + Cele and HFD + Cele-Pro fed mice. Mean ± s.e.m for n = 5, 6, 6, 7. **c**, Free fatty acid (FFA), **(d)** cholesterol (Ch), **(e)** phospholipid (PL) and **(f)** glucose concentrations in mesenteric lymph. Mean ± s.e.m., n = 4, 8, 6, 7 or 4. **g**, Lipidomic analysis heatmap of mesenteric lymph from mice in the prevention study (Fig. 4e,g timeline) or treatment study (Fig. 5a timeline). **h**, Fold change in concentration of significant lipid metabolites in lipidomic analysis including sphingolipids, fatty amides and acyls, glycolipids, sterols, glycerophosphoglycerols, glycerophosphocholines, glycosylphosphatidylinositol, glycerophosphoethanolamines, glycerophosphoinositols in mesenteric lymph from mice in the treatment study (Fig. 5a timeline). **h**, Mean ± s.e.m. of peak intensities from treatment samples multiplied by the fold change values compared to control. n = 4 (CFD), 7 (HFD), 5 (Cele), 3 (Cele-Pro) mice. P values and details of the statistical testing are provided as source data.

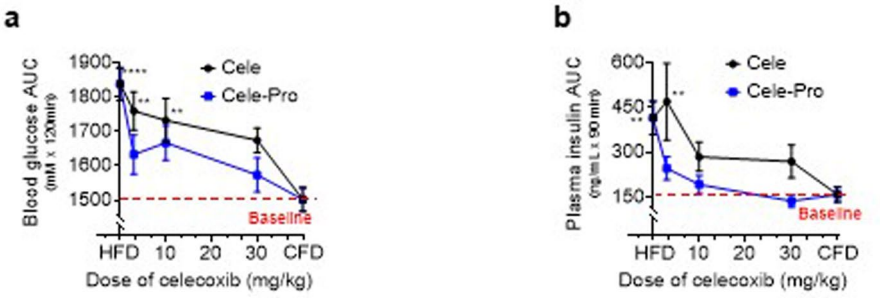


**Extended Data Fig. 8 | Dose-dependent changes to blood glucose and plasma insulin in mice treated with celecoxib or celecoxib prodrug (Cele-Pro).** Blood glucose **(a)** and plasma insulin **(b)** area under the concentration-time curve (AUC) after an oral glucose challenge in mice that were fed with CFD, HFD, HFD + celecoxib (~3, 10, 30 mg/kg) or HFD + Cele-Pro (~3, 10, 30 mg/kg, celecoxib equivalent). Study outline is as described in Fig. 5a. Mean ± s.e.m for CFD (12), HFD (8), HFD + celecoxib (~3 (n = 6), 10 (n = 8), 30 (n = 7) mg/kg) or HFD + Cele-Pro (~3 (n = 7), 10 (n = 6), 30 (n = 8) mg/kg) in **(a)**. CFD (10), HFD (11), HFD + celecoxib (~3 (n = 7), 10 (n = 8), 30 (n = 6) mg/kg) or HFD + Cele-Pro (~3 (n = 7), 10 (n = 6), 30 (n = 8) mg/kg) in **(b)**. Statistical differences, $^{**}p < 0.01$, $^{***}p < 0.005$, or $^{****}p < 0.0001$ from one-way ANOVA compared to CFD. P values and details of the statistical testing are provided as source data.

Corresponding author(s): Natalie Trevaskis
Enyuan Cao
Christopher Porter

Last updated by author(s): Jul 30, 2021

# Reporting Summary

Nature Research wishes to improve the reproducibility of the work that we publish. This form provides structure for consistency and transparency in reporting. For further information on Nature Research policies, see our Editorial Policies and the Editorial Policy Checklist.

## Statistics

For all statistical analyses, confirm that the following items are present in the figure legend, table legend, main text, or Methods section.

| n/a | Confirmed | |
|---|---|---|
| ☐ | ☒ | The exact sample size (*n*) for each experimental group/condition, given as a discrete number and unit of measurement |
| ☐ | ☒ | A statement on whether measurements were taken from distinct samples or whether the same sample was measured repeatedly |
| ☐ | ☒ | The statistical test(s) used AND whether they are one- or two-sided<br>*Only common tests should be described solely by name; describe more complex techniques in the Methods section.* |
| ☐ | ☒ | A description of all covariates tested |
| ☐ | ☒ | A description of any assumptions or corrections, such as tests of normality and adjustment for multiple comparisons |
| ☐ | ☒ | A full description of the statistical parameters including central tendency (e.g. means) or other basic estimates (e.g. regression coefficient) AND variation (e.g. standard deviation) or associated estimates of uncertainty (e.g. confidence intervals) |
| ☐ | ☒ | For null hypothesis testing, the test statistic (e.g. *F*, *t*, *r*) with confidence intervals, effect sizes, degrees of freedom and *P* value noted<br>*Give P values as exact values whenever suitable.* |
| ☒ | ☐ | For Bayesian analysis, information on the choice of priors and Markov chain Monte Carlo settings |
| ☒ | ☐ | For hierarchical and complex designs, identification of the appropriate level for tests and full reporting of outcomes |
| ☐ | ☒ | Estimates of effect sizes (e.g. Cohen's *d*, Pearson's *r*), indicating how they were calculated |

*Our web collection on statistics for biologists contains articles on many of the points above.*

## Software and code

Policy information about availability of computer code

| | |
|---|---|
| Data collection | ImspectorPro software (LaVision Biotec, Bielefeld, Germany), Leica SP8 inverted confocal microscope controlled by LAS AF (version 3.5.5) image acquisition and 2 processing software (Leica, Wetzlar, Germany), BD FACS Canto II (BD Biosciences, Franklin Lakes, NJ, USA), Beckman CoulterMoFlo Astrios cell sorter (CA, USA), Q-Exactive MS (Thermo Scientific, Australia), Operetta high-content imaging system (PerkinElmer), Comprehensive Laboratory Animal Monitoring System (Promethion, Sable Systems, NV, USA), Shimadzu LC-MS 8050 system (Shimadzu Scientific Instruments, Kyoto, Japan), EchoMRITM body composition analyser (EchoMRI, Houstan, TX, USA) |
| Data analysis | Imaris x64 software (version 8.0.1, Bitplane, Zurich, Switzerland), Image J 1.7v Fiji distribution, FlowJo software version 10 (Tree Star Inc., Ashland, OR, USA), IDEOM software, Metaboanalyst, Microsoft Excel, Graphpad Prism version 8 and 9 (GraphPad Software Inc., La Jolla, CA, USA) |

For manuscripts utilizing custom algorithms or software that are central to the research but not yet described in published literature, software must be made available to editors and reviewers. We strongly encourage code deposition in a community repository (e.g. GitHub). See the Nature Research guidelines for submitting code & software for further information.

## Data

Policy information about availability of data

All manuscripts must include a data availability statement. This statement should provide the following information, where applicable:

- Accession codes, unique identifiers, or web links for publicly available datasets
- A list of figures that have associated raw data
- A description of any restrictions on data availability

A data availability statement is included in the manuscript which states: All data generated or analysed during this study are included in this published article (and its

supplementary information and source data files). The data that support the findings of this study are available from the corresponding authors upon request. The exception is the lipidomics data which will be available in the NIH Metabolomics Workbench repository http://dx.doi.org/10.21228/M8GH59.

# Field-specific reporting

Please select the one below that is the best fit for your research. If you are not sure, read the appropriate sections before making your selection.

☒ Life sciences ☐ Behavioural & social sciences ☐ Ecological, evolutionary & environmental sciences

For a reference copy of the document with all sections, see nature.com/documents/nr-reporting-summary-flat.pdf

# Life sciences study design

All studies must disclose on these points even when the disclosure is negative.

| | |
|---|---|
| Sample size | No power calculations were performed prior to the initiation of the study to determine sample size. The animal models used in this study are well established and yield low variance. The sample size was chosen based on previous experience to assure statistical significances and the reproducibility of the results. The number of mice used for each experiment also respected the guidelines of the animal ethics committee. The sample size for human studies was based on power calculations but ultimately limited by patient recruitment due to COVID-19 restrictions. |
| Data exclusions | We did not exclude any experimental sets for mouse experiments. We did not choose specific tissue/cells for experiments. Data from all experimental mice were analysed and included in the results, unless they did not have efficient yield/detection.<br>For mesenteric lymph fluid analysis, lymph with visible blood contamination was excluded. For the oral glucose tolerance test, mice that were stressed (indicated by biting, behaving aggressively, running excessively) were excluded as this raises blood glucose. This is indicated in Figure 6. |
| Replication | Replicates were performed as indicated in the figure legends. In vitro studies were replicated successfully in two to three independent experiments. In vivo studies were replicated and staggered over time. All attempts at replication were successful. |
| Randomization | Allocation of animals into experimental groups was randomised. Control vs high fat diet (+/-treatment) fed animals were age matched throughout all studies. Number of participants for the human study was very low and sporadic such that randomisation was not possible. |
| Blinding | Blinding is not applicable in experiments involving feeding rodents control vs high fat diet (+/-treatment) due to differences in body sizes. Collected lymph and adipose tissue also appears visibly different in obese mice.<br>Blinding is not applicable in human sample collection as both patients that are lean and obese need to meet selection criteria.<br>A fully informed data analysis was performed as described in the Methods. |

# Reporting for specific materials, systems and methods

We require information from authors about some types of materials, experimental systems and methods used in many studies. Here, indicate whether each material, system or method listed is relevant to your study. If you are not sure if a list item applies to your research, read the appropriate section before selecting a response.

## Materials & experimental systems

| n/a | Involved in the study |
|---|---|
| ☐ | ☒ Antibodies |
| ☐ | ☒ Eukaryotic cell lines |
| ☒ | ☐ Palaeontology and archaeology |
| ☐ | ☒ Animals and other organisms |
| ☐ | ☒ Human research participants |
| ☒ | ☐ Clinical data |
| ☒ | ☐ Dual use research of concern |

## Methods

| n/a | Involved in the study |
|---|---|
| ☒ | ☐ ChIP-seq |
| ☐ | ☒ Flow cytometry |
| ☒ | ☐ MRI-based neuroimaging |

## Antibodies

| | |
|---|---|
| Antibodies used | All details of antibodies including clone, dilution/concentration and supplier are listed in Table S3 and Table S5 in the supplementary information.<br>Rabbit anti-LYVE-1 Polyclonal 0.4 µg/mL, 70R-LR005, Fitzgerald, MA, USA<br>Rat anti-CD31 MEC13.3 2.5 µg/mL, 550274, BD Biosciences, NSW, Australia<br>Rat anti-CD11b M1/70 2.5 µg/mL , 101201, BioLegend, CA, USA<br>Rat anti-B220 RA3-6B2 2.5 µg/mL, 103201, BioLegend, CA, USA<br>Rat anti-CD4 RM4-4 2.5 µg/m, 100505, BioLegend, CA, USA<br>Mouse anti-alpha SMA-Cy3 1A4 1-1.5 µg/ml, C6198, Sigma, MO, USA<br>Dylight 405 goat anti-rat antibody 2 µg/mL, 112-475-167, Jackson ImmunoResearch Laboratories Inc., PA, USA<br>Alexa Fluoro 488 goat anti-rabbit antibody 2 µg/mL, A27034, Invitrogen, CA, USA |

Alexa Fluoro 488 goat anti-rat antibody 2 µg/mL ,A-11006, Invitrogen, CA, USA
Alexa Fluoro 647 goat anti-rabbit antibody 2 µg/mL Invitrogen, CA, USA
Alexa Fluoro 647 goat anti-rat antibody 2 µg/mL, A-21245, Invitrogen, CA, USA
Alexa Fluoro 568 goat anti-rat antibody 1 µg/mL, A-11077, Invitrogen, CA, USA
Goat anti-rat Fab fragments 10 µg/mL , 112-006-003, Jackson ImmunoResearch Laboratories Inc., PA, USA
CD11c Armenian hamster IgG N418, 25-0114-82, eBioscience
CD11b Rat IgG2b, κ M1/70, 550993, BD Biosciences
CD19 Rat IgG2a, kappa 6D5, 115511 or 115505, Biolegend
CD3 Rat IgG2b, kappa 17A2, 48-0032-82, eBioscience
CD4 Rat IgG2a, kappa RM4-5, 100525, 100433 or 100509, eBioscience
CD44 Rat IgG2b 1M7, 45-0441-82, eBioscience
CD45 Rat IgG2b, kappa 30-F11, 103126, Biolegend
CD62L Rat IgG2a, kappa MEL-14, 12-0621-82, eBioscience
CD8a Rat IgG2a, kappa 53-6.7, 100711 or 100751, Biolegend
CD8a Rat IgG2a, kappa 53-6.7, 560776, BD Biosciences
F4/80 Rat IgG2a, kappa BM8, 560776, Biolegend
fixable viability dye -65-0865-14 or 65-0866-14 - eBioscience
Ly6G Rat IgG2a, kappa 1A8, 128017, Biolegend
Podoplanin Syrian Hamster IgG 8.1.1, 127411, Biolegend
LYVE1 Rat IgG1, kappa ALY7, 50-0443-80, eBioscience
NK1.1 Mouse IgG2a, kappa PK136, 108723, Biolegend
IL-4 Rat IgG2b, kappa 11b11,504105, BD Biosciences
IL-17A Rat IgG2a, kappa TC11-18H10.1, 506903, BD Biosciences
IFNγ Rat IgG2a, kappa XMG1.2, 505821, BD Biosciences
IgM Rat IgG2a, kappa RMM-1, 406511, Biolegend
IgD Rat IgG2a, kappa 11-26c.2a, 405711, Biolegend

Validation

All antibodies are commercially available and were used for the applications validated by the suppliers. Validation procedures are available on the website of the manufacturers.

## Eukaryotic cell lines

Policy information about cell lines

Cell line source(s)

Lymphatic endothelial cells (LECs) from adult human skin (HMLEC-dLyAd) were purchased from Lonza (Australia)
3T3-L1 cells (ATCC® CL-173™) were kindly provided by Prof Matthew Watt (Australia)

Authentication

The cell lines were not authenticated

Mycoplasma contamination

Cells were not tested for mycoplasma contamination

Commonly misidentified lines
(See ICLAC register)

No commonly misidentified lines were used in the study

## Animals and other organisms

Policy information about studies involving animals; ARRIVE guidelines recommended for reporting animal research

Laboratory animals

Male Sprague Dawley rats or C57BL6/J mice were obtained from the Monash Animal Research Platform. Age was from 6 weeks to 40 weeks. Animals are housed under the following condition: 12h light/12h dark cycle, 22-25C and 35-37% humidity.

Wild animals

No wild animals were used in this project

Field-collected samples

None

Ethics oversight

All animal work was approved by the Monash Institute of Pharmaceutical Sciences Animal Ethics Committee (Projects 13046, 13066 and 24693) and conducted per Australian National Health and Medical Research Council (NHMRC) guidelines

Note that full information on the approval of the study protocol must also be provided in the manuscript.

## Human research participants

Policy information about studies involving human research participants

Population characteristics

Lymph collection patient was from an male patient with obesity
Adipose tissue collection criteria were as follows:
Patients with obesity:
General criteria
Waist circumference >80cm (female) or >94cm (male)
Body mass index (BMI) >30
Two of the following criteria:
Fasting triglycerides >1.7mmol/L
Fasting HDL <1.29mmol/L or
Administration of lipid lowering medication

| | |
|---|---|
| | Systolic blood pressure (BP) >130<br>Diastolic BP >85 or<br>Administration of antihypertensive medication<br>Fasting glucose >5.5mmol/L or<br>Administration of glucose lowering medication<br>Lean patients:<br>General criteria<br>Waist <80cm (female) and <94cm (male) and no history of diabetes<br>BMI <28<br>Exclusions for both obese and lean patients: BMI between 28-30, <18 or >80 years old, pregnancy, Type 1 diabetes, previous laparotomy or small bowel resection, revision Roux-en-Y surgery, anti-inflammatory drug treatment (NSAIDs, COX-2 inhibitors or aspirin for >1 week in last 4 weeks), hypersensitivity to blue dyes (triphenylmethane) or atopic patients with drug allergies<br>Images were from two obese patients (patient 1 female 31 yo; patient 2 female, 41 yo) and three lean patients (patient 1 male, 70 yo; patient 2 female 49 yo; patient 3 female 75 yo). |
| Recruitment | Lymph collection patients: The patient was identified from surgical lists for Ivor Lewis oesophagogastrectomy to resect an adenocarcinoma of the distal oesophagus. The patient was approached regarding recruitment by the operating surgeons. Informed consent took place before starving for surgery and pre-medication.<br>Adipose tissue collection patients: Patients were identified in the Upper GI / Bariatric and Pancreatic Clinics at Greenlane Clinical Centre, Auckland, NZ. They were on the waiting list for an operation that involves the formation of a Roux en Y jejunal anastomosis. Patients were approached regarding recruitment by the clinical research nurse or operating surgeon. Informed consent took place before patients were starved for surgery, without pre-medication and typically in the outpatients clinic prior to admission. Informed consent was the responsibility of the operating surgeon or principle investigator. |
| Ethics oversight | The human studies were approved by the New Zealand Health and Disability Ethics Committees (Approvals 17/NTA/249 and 12/NTB/67, respectively). Informed consent was taken from all patients and no payment was received. |

Note that full information on the approval of the study protocol must also be provided in the manuscript.

# Flow Cytometry

## Plots

Confirm that:

☒ The axis labels state the marker and fluorochrome used (e.g. CD4-FITC).

☒ The axis scales are clearly visible. Include numbers along axes only for bottom left plot of group (a 'group' is an analysis of identical markers).

☒ All plots are contour plots with outliers or pseudocolor plots.

☒ A numerical value for number of cells or percentage (with statistics) is provided.

## Methodology

| | |
|---|---|
| Sample preparation | Cells isolated from lymph, lymph nodes and mesenteric adipose tissue were stained with appropriate antibodies at 4°C for 20 minutes. Excess antibody was washed off and cells were analysed. Viability dye was used to identify dead cells and gated out during analysis. For intracellular staining, surface stained cells were fixed and permeabilised using the Cytofix/Cytoperm kit followed by appropriate antibody staining for 20 min. |
| Instrument | BD FACS Canto II (BD Biosciences, Franklin Lakes, NJ, USA), Beckman Coulter MoFlo Astrios cell sorter (CA, United States) |
| Software | FlowJo software version 10 (Tree Star Inc. Ashland, OR, USA) |
| Cell population abundance | Cell populations analysed ranged from 30000-1000000 cells/tissue/mouse |
| Gating strategy | Appropriate negative, compensation and FMO controls were used in all flow cytometry experiments.<br><br>Lymph and lymph nodes: FSC-A and FSC-H gating were used to discriminate singlets. Viability dye was used to discriminate live/dead cells. CD45+ cells were selected for leukocytes followed by CD3+ cell selection for T cells. T cells were further gated on FSC-A vs IFNg +for Th1 cells, FSC-A vs IL-17+ for Th17 cells and FSC-A vs IL-4+ for Th2 cells. B cells were selected by FSC-A vs CD19+ gating. CD11c+ cells were selected by FSC-A vs CD11c+ gating. F4/80+ cells were selected by FSC-A vs F4/80+ gating and NK cells were selected by FSC-A vs NK1.1+ gating.<br><br>Mesenteric adipose tissue: FSC-A and FSC-H gating were used to discriminate singlets. Viability dye was used to discriminate live/dead cells. CD45+ cells were selected for leukocytes followed by F4/80+ cell selection for macrophages.<br><br>Mesenteric adipose tissue and intestine (lamina propria) cell sorting: FSC-A and FSC-H gating were used to discriminate singlets. Viability dye was used to discriminate live/dead cells. CD45+ cells were selected for leukocytes followed by CD11b +F4/80+ cell selection for macrophages. CD45- cells were further gated on FSC-A vs CD31- cells followed by gating on LYVE-1 +/podoplanin+ cells for lymphatic endothelial cells. |

☒ Tick this box to confirm that a figure exemplifying the gating strategy is provided in the Supplementary Information.